Dalton Transactions

PAPER

View Article Online
View Journal | View Issue

Cite this: *Dalton Trans.*, 2018, **47**, 15596

Mononuclear iron(II) complexes containing a tripodal and macrocyclic nitrogen ligand: synthesis, reactivity and application in cyclohexane oxidation catalysis†‡

Massinisa Ayad,[a] Robertus J. M. Klein Gebbink,[b] Yves Le Mest,[a] Philippe Schollhammer,[a] Nicolas Le Poul,*[a] François Y. Pétillon*[a] and Dominique Mandon§[a]

Received 19th July 2018,
Accepted 28th September 2018

DOI: 10.1039/c8dt02952k

rsc.li/dalton

Two novel tripodal ligands L^1 and L^2 based on a tris(methylpyridyl)amine (TPA) motif have been prepared and reacted with two different iron(II) salts. The ligand L^1 contains a bis(amino-phenyl)-TPA group whereas the macrocyclic ligand L^2 displays two different coordinating cores, namely TPA and pyridine–dicarboxamide. The resulting mononuclear complexes **1–4** have been characterized in the solid state and in solution by spectroscopic and electrochemical methods. All complexes are high spin and mainly penta-coordinated. X-ray diffraction analyses of the crystals of complexes **2** and **3** demonstrate that the coordination sphere of the iron(II) centre adopts either a distorted bipyramidal–trigonal or square pyramidal geometry. In the absence of an exogenous substrate, oxidation of complex **2** by H_2O_2 induces an intramolecular aromatic hydroxylation, as shown by the X-ray structure of the resulting dinuclear complex **2′**. Catalytic studies in the presence of a substrate (cyclohexane) show that the reaction process is strongly impacted by the macrocyclic topology of the ligand and the nature of the counter-ion.

Introduction

Most of the oxidation reactions occurring in Nature are catalysed by iron enzymes.[1–3] On one hand, heme-enzymes such as cytochrome P450 have been extensively studied because of their ubiquitous roles in many reactions occurring in plants, bacteria and animals.[4–6] The large number of in-depth studies has led to the characterization of several reactive iron–oxygen adducts, such as iron-hydroperoxo and iron-oxo species, which have inspired chemists to develop synthetic model complexes based on heme-like ligands, such as porphyrins, phthalocyanins or corroles.[7,8] On the other hand, non-heme iron enzymes have generated particular interest for the last twenty years.[9–13] Among them, mononuclear Rieske dioxygenases[14–16] and dinuclear soluble methane monooxygenases (sMMOs)[3,9,17–19] have been widely investigated because these enzymes can take part in the hydroxylation of aromatic and aliphatic hydrocarbons, respectively. Most of the mononuclear non-heme iron enzymes display two histidine residues and labile water molecules in their active sites, the coordination sphere being completed by aspartate or glutamate groups, known as the 2-His-1-carboxylate triad.[13,14] For instance, naphthalene 1,2-dioxygenase catalyzes the *cis*-hydroxylation of naphthalene by reaction of a pentacoordinated Fe(II) centre with O_2. The reaction occurs through the formation of putative $Fe^{V}(O)(OH)$ adducts resulting from the O–O bond cleavage of hydroperoxo $Fe^{III}(OOH)$ species.[2,14] Dinuclear non-heme enzymes display another mode of processing catalytic oxidations.[9] Hence, sMMOs are characterized in their resting state in their active site by a $[Fe_2^{III}(\mu\text{-}OH)_2]$ cluster surrounded by glutamate and histidine moieties. In the (**II**,**II**) reduced state, a reaction with O_2 leads to the formation of transient iron–oxygen species. Among them, the "diamond core" bis-μ-oxo Fe_2^{IV} (Q") was shown to be one key active species that takes part in the oxidation of methane into methanol.[1,2,17] Recent studies on particulate methane monooxygenases (pMMOs) have emphasized the importance of the MMOB (methane monooxygenase B) sub-unit in the

[a]*UMR CNRS 6521, Laboratoire de Chimie, Electrochimie Moléculaires et Chimie Analytique, Université de Bretagne Occidentale, 6 Avenue Victor Le Gorgeu, CS 93837, 29238 Brest Cedex 3, France. E-mail: francois.petillon@univ-brest.fr, nicolas.lepoul@univ-brest.fr*

[b]*Organic Chemistry and Catalysis, Debye Institute for Nanomaterials Science, Universiteit Utrecht, Universiteitsweg 99, 3584 CG, Utrecht, The Netherlands*

†This article is dedicated to the memory of Prof. Jacques E. Guerchais, who passed away in April 2018.

‡Electronic supplementary information (ESI) available: UV-Vis spectroscopic and X-ray data. CCDC 1856876–1856878. For ESI and crystallographic data in CIF or other electronic format see DOI: 10.1039/c8dt02952k

§Passed away in July 2016.

catalytic process for both triggering the substrate and dioxygen transport through the protein pores and inhibiting further reduction of the generated Fe_2O_2 cluster.[3]

Many synthetic models of non-heme iron enzymes have been developed over almost thirty years in order to obtain efficient catalysts for hydrocarbon oxidation.[2,7,9,18] Different ligand architectures have been proposed according to the targeted transient mononuclear or dinuclear iron–oxygen species. Among them, two examples of widely studied monotopic ligand families can be mentioned, namely the tripodal tetradentate TPA moiety (TPA = tris(methylpyridine)amine) and the multidentate macrocyclic cyclam or TACN series (cyclam = tetraazacyclotetradecane, TACN = triazacyclononane). Hence, Que *et al*. reported in 1999 the first crystallographic evidence of a "diamond core" $Fe^{IV}Fe^{III}(\mu\text{-}O)_2$ complex by appropriate design of a TPA ligand (5-Et_3TPA).[20] Since then, many other monotopic TPA-based ligands have been described, leading to mono- or bis-iron complexes.[9,21] Alternatively, monotopic cyclam-based ligands have also been widely developed.[22–24] Structures of different mononuclear iron–oxygen adducts (Fe^{III} peroxo and Fe^{IV} oxo) were obtained with the *N*-substituted cyclam derivative.[22,24–26] Concomitantly, Costas and co-workers investigated the iron chemistry of *N*-substituted TACN ligands.[2,27] A mononuclear $Fe^{V}(O)(OH)$ adduct was characterized by mass spectrometry from the reaction of the $[Fe^{II}(^{Me,HPy}TACN)(OTf)_2]$ complex (OTf^- = triflate ion) with hydrogen peroxide.[28]

Since, other high-valent species have been identified. Moreover, the role of water in the formation of such species has been emphasized ("water-assisted mechanism").[2,9] Ditopic ligands have also been designed in order to mimic the active site of sMMOs.[1,18,29–33] These are based on pincer-type moieties in order to adjust the Fe–Fe distance by bridging groups (carboxylate, benzoate, *etc*.). For instance, Kodera and co-workers used a bis-TPA frame in order to obtain a high-spin (S = 2) $Fe^{IV}_2(\mu\text{-}O)$ adduct.[34] Alternatively, Lippard *et al*. synthesised a pre-organized macrocyclic ditopic ligand bearing two phenoxylimine (PIM) coordinating cores.[35,36] The latter authors showed very recently that the redox properties of the bis-iron complexes could be tuned by suitable introduction of a carboxylate group in the PIM moiety.[37] For all these model complexes, many parameters have been varied in order to rationalize the effect of the ligand topology on the catalytic properties.[2,9,38] Hence, high-spin iron complexes displaying labile ligands in the *cis*-position and high redox potential have been targeted. High reactivity was obtained from high-spin (S = 2) mononuclear Fe^{IV}-oxo species generated by using bulky tripodal moieties and weak-field equatorial ligands.[39]

Inspired by the recent work on the structural models of sMMOs developed by Lippard and co-workers, we have focused our research on the development of a macrocyclic ligand which could display one or two coordination sites for metal ions. By taking advantage of our previous work on TPA-derivatives and their mononuclear complexes,[40–50] we have designed a novel ligand $\mathbf{L^2}$ (Chart 1) which displays two different coordinating cores, namely TPA and pyridine–dicarboxamide (PydCA). Such a dissymmetrical ditopic ligand may indeed coordinate one or several metal ions, leading to the formation of homo or hetero-

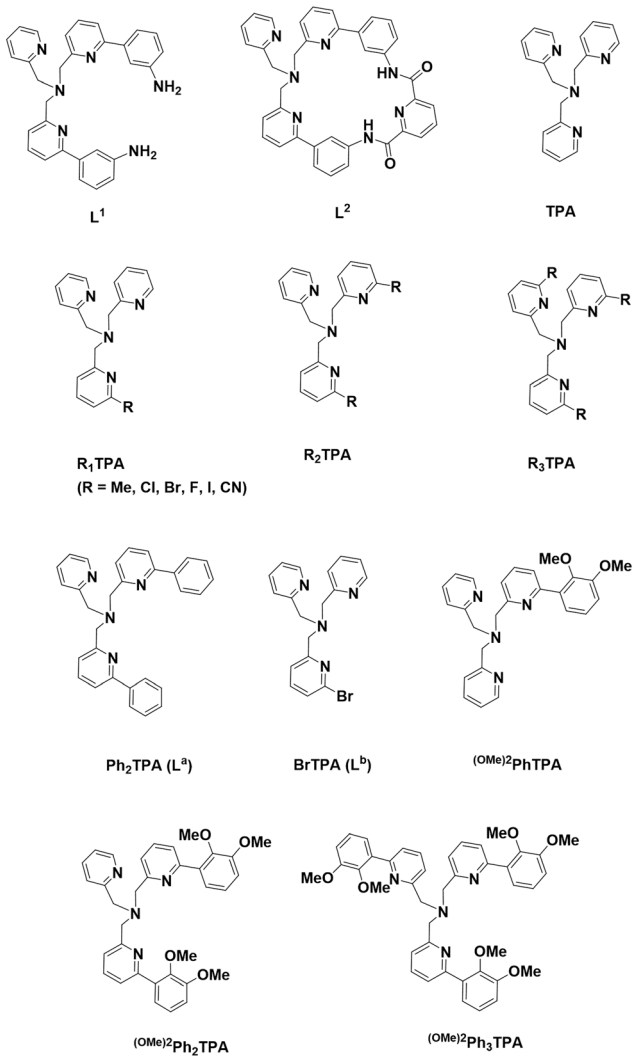

Chart 1

nuclear dinuclear complexes as recently reported for analogous macrocyclic ligands.[51–53] We thus present here the synthesis and characterization of the ligand $\mathbf{L^2}$ and its precursor $\mathbf{L^1}$ (Chart 1). Based on the first results, we have focused our work on mononuclear iron(II) complexes **1–4** derived from these two ligands, and scrutinized the effect of the counter-ion (chloride, triflate) and the topology of the ligand on the structural properties and reactivity toward oxidants (O_2, H_2O_2, *m*-chloroperoxybenzoic acid (*m*-CPBA)) in the absence and presence of a hydrogenated substrate (cyclohexane). A comparison with analogous iron complexes bearing TPA-derived ligands (Chart 1) has been carried out to better account for the effects of the ligand architecture on the catalytic properties.

Experimental section

General procedures

All air sensitive organic reactions, as well as the handling and synthesis of iron complexes were routinely carried out under

an argon atmosphere using standard Schlenk techniques. Further manipulations were performed in an MBraun UNILab sp glovebox workstation under an argon atmosphere, unless otherwise pointed out. Solvents were either distilled immediately before use under nitrogen from appropriate drying agents or passed through an MBraun MB SPS-800 solvent purification system. All dry solvents were degassed before use by bubbling N_2 through the liquid for 30 min or by freeze–thawing with liquid nitrogen under strict anaerobic conditions. Methanol was rigorously dried with Mg turnings; CH_2Cl_2 (electrochemistry) was freshly distilled from CaH_2 and kept under Ar in a glovebox. The precursors 2-methyl-6 bromo-pyridine,[54] 6-bromo-2-(bromomethyl)pyridine,[55] and bis{(6-bromo-2-pyridyl)methyl}(2-pyridylmethyl)amine[45,56,57] were prepared according to previously described methods. All other reagents were purchased from Sigma-Aldrich and used without purification. Column chromatography was performed using silica gel (60–200 μm, 60 Å) or neutral activated aluminum oxide (50–160 mm).

Physical methods

Infrared spectra were recorded on a Bruker-Vertex 70-Avatar spectrometer for solids. Chemical analyses were performed either by the 'Service de Microanalyse' ICSN-CNRS of Gif/Yvette (France) or by the "Service Central d'Analyse" of Vernaison (France). UV-Vis measurements were carried out on a Jasco V-650 (190–1000 mm) spectrophotometer or a Varian Cary 05 E UV-VIS NIR spectrophotometer equipped with an Oxford instrument DN 1704 cryostat in optically transparent Schlenk cells. NMR spectra were recorded in $CDCl_3$, CD_3CN or CD_2Cl_2 at ambient temperature on a Bruker AC 500 (^{1}H, ^{13}C), AC 400 (^{1}H, ^{13}C, ^{31}P), or AC 300 (^{1}H, ^{13}C, ^{31}P, ^{19}F) spectrometer, according to the sample that was analyzed; the signals are indicated as follows: chemical shift (ppm), intensity, multiplicity, and coupling constants (J, Hz). EPR spectra were obtained on a Bruker Elexsys E500 spectrometer, at a perpendicular mode X band (9.62 GHZ); simulations were performed using the Bruker Spin-Count software. Electrochemical studies of the complexes were performed in a glovebox (Jacomex) (O_2 < 1 ppm, H_2O < 1 ppm) with a home-designed 3-electrode cell (WE: glassy carbon, RE: Pt wire in a Fc^+/Fc solution, CE: Pt or a graphite rod). Ferrocene was added at the end of the experiments to determine redox potential values. The potential of the cell was controlled by using an AUTOLAB PGSTAT 100 (Metrohm) potentiostat monitored by the NOVA software. HPLC-grade acetonitrile was degassed under argon and stored in a glovebox. Dichloromethane was distilled over CaH_2 before being stored in a glovebox. The supporting salt NBu_4PF_6 was synthesized from NBu_4OH (Acros) and HPF_6 (Aldrich). It was then purified, dried under vacuum for 48 hours at 100° C, and then kept under argon in a glovebox. Conductivity measurements were carried out under argon at 20 °C in CH_3CN with a CDM 210 Radiometer Copenhagen Conductivity Meter using a Tacussel XE 150 507569 electrode; the procedure used for the complexes was the following: 4 mL of dry and degasified acetonitrile were introduced into the cell and the relative conductivity of the blank was measured (A), and then the relative conductivity of the sample in CH_3CN was determined (B), giving the conductivity values of the complex by subtraction (B–A/concentration). Mass spectrometric measurements were performed on an Autoflex MALDI TOF III LRF200 spectrometer by the "Service Commun de Spectrométrie de Masse" of the University of Bretagne Occidentale (Brest). ESI-MS spectrometry was performed on a Waters LCT Premier XE KE317 Micromass Technologies spectrometer at the Debye Institute for Nanomaterials Science, Faculty of Science, Utrecht University, The Netherlands. GC analysis was performed with a PerkinElmer Clarus 500 gas chromatograph equipped with an Agilent HP-5 column (30 m × 0.32 mm × 0.25 μm) and a flame-ionization detector at the Debye Institute for Nanomaterials Science (Utrecht), the Netherlands.

Synthesis of the ligands

L^1. The ligand L^1 was synthesized according to the Suzuki cross-coupling procedure.[57–59] To a mixture of 500 mg (1.12 mmol) of bis{(6-bromo-2-pyridyl)methyl}(2-pyridylmethyl)amine (α-Br_2-TPA) and 174 mg (1.12 mmol) of $[Pd(PPh_3)_4]$ in 100 mL of degassed toluene were added 10 mL of a 0.1 M solution of $K_2(CO_3)$ and 2.5 eq. of 2-aminophenyl boronic acid (363 mg, 2.35 mmol) in suspension in 10 mL of degassed ethanol. The mixture, kept under an argon atmosphere, was heated to reflux at 120 °C and stirred for 48 h. Then, the solution was evaporated to dryness to give a pale-yellow oil. The residue was taken up from CH_2Cl_2 and washed several times with aqueous $K_2(CO_3)$, and then with water. The organic layer was dried over magnesium sulfate, and then concentrated. Addition of pentane gave a brown residue, which was dissolved in CH_2Cl_2. This procedure was repeated three times. Thus, the resulting brown oil turned out to be the clean product L^1 ($C_{30}H_{28}N_6$). Yield 320 mg (60%). ^{1}H-NMR (400 MHz, $CDCl_3$, δ): 8.47(d, J = 5.6 Hz, 1H), 7.69–7.64(m, 6H), 7.55(t, J = 4.4 Hz, 5H), 7.48(dt, J^3 = 7.6 Hz, J^4 = 2.8 Hz, 1H), 7.39(t, J = 2.0 Hz, 1H), 7.32(d, J = 7.6 Hz, 2H), 7.13(t, J = 4.8 Hz, 1H), 6.71(dd, J^3 = 7.6 Hz, J^4 = 0.8 Hz, 1H), 4.01(s, 4H), 4.00(s, 2H), 3.74(s, 4H). ^{13}C-NMR (75.46 MHz, $CDCl_3$, δ): 161.2(C_{ipso}), 160.6(C_{ipso}), 158.1(C_{ipso}), 150.4(CH), 148.3(C_{ipso}), 141.9(C_{ipso}), 138.3(C_{ipso}), 137.8(CH), 133.5(CH), 133.4(CH), 129.9(CH), 129.8 (CH), 129.6(CH), 124.3(CH), 123.3(CH), 122.5(CH), 120.1(CH), 118.5(CH), 117.0(CH), 115.0(CH), 61.8(2C, C_{meso}, N–CH_2–Py), 61.7(1C, C_{meso}, N–CH_2–Py).

L^2. The ligand L^2 was synthesized according to a slightly modified method of Holm *et al.*[52] To a dried THF (500 mL) solution of Et_3N (3 mL, 40 eq.) was added simultaneously a THF solution (50 mL) of 2,6-pyridine dicarbonylchloride (260 mg, 1.27 mmol) and 2-aminophenyl-6-methylpyridine (500 mg, 1.05 mmol) in THF/acetonitrile (50 mL, 4/1) drop by drop over 3 h. The mixture was refluxed at 120 °C for 3 days, and filtered. Then, the volatiles were evaporated to give a brown oil, which was dissolved in dichloromethane (10 mL) and dried over $MgSO_4$. After filtration and evaporation of the solvent, the product was purified by crystallization in dichloromethane/pentane (5/95) to give L^2 ($C_{37}H_{29}N_7O_2$) as a light

brown powder. Yield 325 mg (51%). IR (solid, cm^{-1}): ν(NH) 3313(w), ν(C=O) 1681(s). ^{1}H-NMR (400 MHz, $CDCl_3$, δ): 10.31 (s, 2H), 8.61(d, J = 6.5 Hz, 2H), 8.56(d, J = 8.0 Hz, 1H), 8.14(t, J = 8.0 Hz, 1H), 7.70(t, J = 7.6 Hz, 3H), 7.55(m, 10H), 7.31(d, J = 7.0 Hz, 3H), 6.99(t, J = 5.6 Hz, 1H), 4.17(s, 4H), 4.13(s, 2H). ^{13}C-NMR (75.46 MHz, $CDCl_3$, δ): 161.1(2C, *C*=O), 159.3(2C, C_{ipso}), 158.0(2C, C_{ipso}), 156.2(2C, *C*=O), 148.4(2C, C_{ipso}), 148.2 (1C, CH), 139.6(2C, C_{ipso}), 138.3(1C, *C*H), 137.2(2C, C_{ipso}), 136.7 (2C, *C*H), 135.8(1C, *C*H), 128.7(2C, *C*H), 122.5(1C, *C*H), 124.9 (2C, *C*H), 121.9(2C, *C*H), 121.3(2C, *C*H), 120.1(1C, *C*H), 119.4 (2C, *C*H), 118.9(4C, *C*H), 61.6(2C, C_{meso}, N–*C*H$_2$–Py), 59.8(1C, C_{meso}, N–*C*H$_2$–Py). ESI-MS ($CHCl_3$, m/z): calcd for [M]: 603.31. Found: 602.13 assigned to $[M - H]^+$.

Synthesis of iron(II) complexes

[FeCl$_2$(L^1)] (1). To a yellow-brown solution of **L^1** (80 mg, 0.17 mmol) in dry, degassed CH_3CN (5 mL) was added a light-yellow suspension of anhydrous $FeCl_2$ (20.4 mg, 0.16 mmol) in acetonitrile (5 mL) at room temperature; upon addition, the solution colour changed to orange. The reaction mixture was stirred for 8 h and then concentrated under reduced pressure. Addition of Et_2O (30 mL) afforded a green solid, which was washed with Et_2O (3 × 10 mL), and then dried under vacuum to give **1** as a dark-green powder. Yield 73 mg (76%). ^{1}H-NMR (400 MHz, CD_2Cl_2, δ) (ppm): 119.2(s-br, 1H, C*H*$_{\alpha(Pyr)}$), 86.1(s-br, 2H, C*H*$_2$), 53.8(s, 1H, C*H*$_{\beta,\beta'(Pyr)}$), 51.2(s, 1H, C*H*$_{\beta,\beta'(Pyr)}$), 32.2 (s-br, 2H, C*H*$_2$), 17.3(s-br, 2H, C*H*$_2$), 7.3(m, 3H, C*H*$_{\gamma(Pyr)}$), 3.9(s-br, 1H, C*H*$_{\gamma(Pyr)}$), 1.3(s, 2H, N*H*$_2$), 1.1(s, 2H, N*H*$_2$), 0.57(s-br, 3H, uncoord. Pyr). UV-Vis (MeCN) λ_{max}, nm (ε, M^{-1} cm^{-1}): 257 (18550), 285(14 500), 324(8160). ESI-MS (CH_3CN, m/z): calcd for $[FeCl(L^1)]^+$: 563.14. Found: 563.13.

[FeCl$_2$(L^2)] (2). To an acetonitrile (10 mL) solution of **L^2** (100 mg, 0.16 mmol) was added, under argon, 20 mg (0.16 mmol) of anhydrous $FeCl_2$ in degassed CH_3CN (10 mL). The mixture was stirred overnight and then concentrated under reduced pressure. Addition of diethyl ether afforded a yellow-brown powder. Crystals suitable for an X-ray analysis were formed by slow vapour diffusion of Et_2O into a CH_2Cl_2 solution of **2** in a sealed tube. Yield 73 mg (62%). Anal. found: C = 58.31, H = 3.87, N = 12.43%. Anal. calcd for $C_{37}H_{29}Cl_2FeN_7O_2$, 1.5 H_2O (757.08): C = 58.65, H = 4.26, N = 12.94%. IR (solid, cm^{-1}): ν(NH) 3446(w), ν(CO) 1683(s). ^{1}H-NMR (300 MHz, CD_3CN, δ) (ppm): 102.2(s-vbr, 1H, C*H*$_{\alpha(Pyr)}$), 53.7(s-vbr, 2H, C*H*$_2$), 45.7(s, 1H, C*H*$_{\beta,\beta'(Pyr)}$), 42.4(s, 1H, C*H*$_{\beta,\beta'(Pyr)}$), 38.4(s-vbr, 2H, C*H*$_2$), 33.3(s-br, 2H, C*H*$_2$), 29.9(s, 2H, C*H*$_{\beta,\beta'(Pyr)}$), 11.7(s, 1H, C*H*$_{\gamma(Pyr)}$), 7.9(m, 8H, C*H*$_{(Phenyl\ subst.)}$), 3.9(s, 1H, C*H*$_{\gamma(Pyr)}$), 2.7(s), 0.35(s) and −2.7(s) (6H, C*H*$_{\beta,\beta'',\gamma(uncord.\ Pyr)}$), −8.7(s, 2H, N*H*). UV-Vis (CH_2Cl_2) λ_{max}, nm (ε, M^{-1} cm^{-1}): 253(10 500), 341(3280), 386(1785). ESI-MS ($CHCl_3$, m/z): calcd for $[FeCl(L^2)]^+$: 694.62. Found: 694.66. Molecular conductivity (C = 1.5 mM, CH_3CN): Λ = 24 S cm^2 mol^{-1}. Magnetic moment (Evan's method):[60,61] μ_{eff} = 1.52μ_B.

[Fe^{III}(OH)(OL$^{2'}$)]$_2$[(FeCl$_3$)$_2$(μ-O)]·3CH$_3$CN (2′); L$^{2'}$ = L^2–1H$_{Ph}$. To an acetonitrile (3 mL) solution of **2** (8 mg, 0.01 mmol) were added 10 eq. of H_2O_2 (33%) in CH_3CN. After stirring for a few minutes, the colour turned from yellow-brown to red-orange. The solvent was then removed giving small amounts of **2′** as a red-orange powder, which was recrystallized by slow diffusion of Et_2O into an acetonitrile solution of **2′** giving, after several days, single crystals suitable for X-ray analysis. EPR (9.30 GHz, CH_3CN, 150 K): silent.

[Fe(CH$_3$CN)(L^1)](OTf)$_2$ (3). A white suspension of [Fe(OTf)$_2$] (71.2 mg, 0.20 mmol) in dry, degassed CH_3CN (5 mL) was added to an acetonitrile (5 mL) solution of **L^1** (100 mg, 0.21 mmol) under argon, at room temperature. Upon addition, the colour of the reaction mixture changed to red-orange. After stirring for 8 h, a red-brown solid was formed. The solvent was removed by cannula filtration and the product was washed with Et_2O (3 × 10 mL), and then dried in a vacuum to give **3** as a red-orange powder. Crystals suitable for an X-ray analysis were obtained by slow vapour diffusion of Et_2O into a CH_3CN solution of **3**, in a sealed tube. Yield 86 mg (52%). IR (solid, cm^{-1}): ν(NH) 3360(s), ν(CF) 1026(s). ^{1}H-NMR (400 MHz, δ) (ppm): 120.1(s-vbr, 1H, C*H*$_{\alpha(Pyr)}$), 61.4(s-br, 2H, C*H*$_2$), 60.7(s-br, 3H, C*H*$_{\beta,\beta'(Pyr)}$), 59.1(s-br, 2H, C*H*$_2$), 46.5(s-br, 3H, C*H*$_{\beta,\beta'(Pyr)}$), 20.6(s-vbr, 3H, C*H*$_{\gamma(Pyr)}$), 11.5(s-br, 3H, C*H*$_{(Phenyl\ subst.)}$), 7.3(m-br, 3H, C*H*$_{(Phenyl\ subst.)}$), 5.45(s, 2H, C*H*$_{(Phenyl\ subst.)}$), 3.6(s, 3H, C*H*$_3$CN), −9.8(s, 2H, C*H*$_2$), −12.0(s, 4H, N*H*$_2$). ^{19}F-NMR (282.23 MHz, CD_3CN, δ) (ppm): −78.2(s, C*F*$_3$). UV-Vis (MeCN) λ_{max}, nm (ε, M^{-1} cm^{-1}): 259(16 300), 283(13 360), 335(4880). ESI-MS (CH_3CN, m/z): calcd for $[Fe(OTf)(L^1)]^+$: 677.12. Found: 677.10.

[Fe(H$_2$O)$_2$(L^2)](OTf)$_2$, 2H$_2$O (4). An acetonitrile solution of [Fe(OTf)$_2$] (35.4 mg, 0.10 mmol) was added to a MeCN (5 mL) solution of **L^2** (100 mg, 0.10 mmol). The mixture was stirred overnight and then filtered. The volume of the solvent was reduced to *ca.* 1 mL. Then, Et_2O (10 mL) was added to precipitate a solid. The solvent was removed by cannula filtration and the product was washed twice with Et_2O (2 × 5 mL), and then dried in a vacuum to give compound **4** as a red-orange solid. Yield 68 mg (~40%). IR (solid, cm^{-1}): ν(NH) 3342(w), ν(CO) 1680(m), ν(CF) 1029(s). ^{1}H-NMR (400 MHz, CD_3CN, δ) (ppm): 62.4(s-vbr, 1H, C*H*$_{\beta,\beta'(Pyr)}$), 46.9(s-br, 1H, C*H*$_{\beta,\beta'(Pyr)}$), 38.2(s-vbr, 2H, C*H*$_2$), 33.0(s-vbr, 2H, C*H*$_2$), 30.5(s-vbr, 2H, C*H*$_{\beta,\beta'(Pyr)}$), 11.7 (s-vbr, 2H, C*H*$_2$), 10.8(s-br, 2H, C*H*$_{(Phenyl\ subst.)}$), 9.2(s-br, 2H, C*H*$\gamma_{(Pyr)}$), 8.7(s-br, 1H, C*H*$\gamma_{(Pyr)}$), 8.3(s-br, 1H, C*H*$_{(Phy\ subst.)}$), 8.0–7.5(m, 3H, C*H*$_{(Phenyl\ subst.)}$), 7.2(s-br, 1H, C*H*$_{(Phenyl\ subst.)}$), 3.9(s-br, 1H, C*H*$_{(Phenyl\ subst.)}$), 2.14(O*H*$_{(H20)}$, obscured by CH_3CN-CD_3CN), 1.28(s-br, 1H, C*H*$_{(uncord.\ Pyr)}$), −0.32(s-br, 2H, C*H*$_{(uncord.\ Pyr)}$), −2.86(s-br, 2H, N*H*$_2$). ^{19}F-NMR (282.23 MHz, CD_3CN, δ) (ppm): −79.6(s, CF_3). UV-Vis (MeCN) λ_{max}, nm (ε, M^{-1} cm^{-1}): 253(18 100), 284(18 600). ESI-MS ($CHCl_3$, m/z): calcd for $[Fe(H_2O)_2(OTf)(L^2)]^+$, 2H_2O: 880.2. Found: 880.2. Molecular conductivity (C = 1.5 mM, CH_3CN): Λ = 138 S cm^2 mol^{-1}.

X-ray structural determination

Measurements for compounds **2**, **2′** and **3** were made on an Oxford Diffraction X-Calibur-2CDD diffractometer equipped with a jet cooler device. Graphite-monochromated Mo Kα radiation (λ = 0.71073 Å) was used in all experiments. The struc-

tures were solved and refined by standard procedures.[62,63] Small crystals were obtained for **2′**; therefore, they gave somewhat low-resolution diffraction patterns. However, the results of the diffraction analysis for this compound **2′** provide sufficient proof of the proposed structure. A nitrogen stream cryostat attached to the system enabled low-temperature measurements (mainly at 170 K).

Intensity data were collected combining several runs (omega-scan, step 1^0) in order to obtain a complete set of reflections (as far as possible down to d = 0.8 Å or less). Selected bond lengths, angles, data collection and processing parameters are given in Table 1 and in the ESI.‡

Catalytic oxidation of cyclohexane

The catalytic properties of the iron(II) complexes for the room temperature oxidation of cyclohexane in the presence of hydrogen peroxide or *m*-CPBA have been investigated by gas-chromatography (GC). Experiments were performed with an excess of the substrate and oxidizing agent (*vs*. catalyst) to avoid the oxidation of the solvent (MeCN) and over-oxidation of the products. The quantitative determination of the main products, cyclohexanol (A) and cyclohexanone (K), was carried out by using acetophenone, as an internal standard compound. Hence, the turnover number (moles of products/moles of catalysts), the alcohol/ketone concentration ratio ([A]/[K]) and the total yield (moles of products/moles of oxidant) have been determined for each catalyst under different experimental conditions. Additionally, control experiments under the same experimental conditions but without catalysts were performed. They indicated that cyclohexane could not be oxidized without the iron(II) precursor.

Results and discussion

Syntheses

The ligands $\mathbf{L^1}$ and $\mathbf{L^2}$ were synthesized and characterized according to procedures similar to those reported previously[52,57–59] (see the Experimental section). Here, these two organic compounds acted either as tridentate or tetradentate ligands depending on the nature of the iron salt that was used as a reactant. Tridentate and tetradentate coordination modes of the ligand were operative, respectively, with [$FeCl_2$] and [$Fe(OTf)_2$]. Thus, treatment of [$FeCl_2$] with 1 eq. of $\mathbf{L^1}$ in acetonitrile at room temperature, under inert conditions, resulted in a clear color change from pale-yellow to orange; after work-up of the reaction product, a dark-green solid **1** was obtained in good yields. In a similar way, a reaction of [$FeCl_2$] with $\mathbf{L^2}$ gave compound **2** as a yellow-brown powder in valuable yields (see Scheme 1(a)). As shown below, both complexes **1** and **2** are neutral, whereas dicationic compounds **3** and **4** were

Table 1 Crystal data and structure refinement for compounds **2**, **2′** and **3** at 170 K

	2	**2′**	**3**
Empirical formula	$C_{37}H_{29}Cl_2FeN_7O_2$	$C_{80}H_{67}Cl_6Fe_4N_{17}O_9$	$C_{34}H_{31}F_6FeN_7O_6S_2$
Formula weight	730.42	1846.61	867.63
Temperature	170(2) K	170(2) K	170(2) K
Wavelength	0.71073 Å	0.71073 Å	0.71073 Å
Crystal system, space group	Monoclinic, *Cc*	Monoclinic, *P*21/*m*	Triclinic, *P*$\bar{1}$
Unit cell dimensions	*a* = 15.153(3) Å *b* = 13.630(2) Å *β* = 107.23(2)° *c* = 16.654(3) Å	*a* = 12.8448(6) Å *b* = 24.3450(14) Å *β* = 110.800(6)° *c* = 13.5498(7) Å	*a* = 11.6048(4) Å *α* = 116.401(4)° *b* = 13.6563(6) Å *β* = 92.178(3)° *c* = 14.1144(4) Å *γ* = 109.682(4)°
Volume	3285.3(10) Å^3	3961.0(4) Å^3	1839.14(12) Å^3
Z, calculated density	4, 1.477 Mg m^{-3}	2, 1.548 Mg m^{-3}	2, 1.567 Mg m^{-3}
Absorption coefficient	0.669 mm^{-1}	0.990 mm^{-1}	0.610 mm^{-1}
F(000)	1504	1888	888
Crystal description	Triangular rod, axis [1 0 0]	Rod, axis [1 0 0]	Fragment of a plate
Crystal colour	Colourless	Brown	Yellow
Crystal size	0.17 × 0.06 × 0.03 mm	0.19 × 0.07 × 0.06 mm	0.33 × 0.18 × 0.13 mm
Theta range for data collection	2.81 to 26.37°	3.31 to 26.37°	3.43 to 26.37°
Limiting indices	$-14 \le h \le 18$, $-16 \le k \le 17$, $-20 \le l \le 20$	$-15 \le h \le 16$, $-20 \le k \le 30$, $-16 \le l \le 16$	$-12 \le h \le 14$, $-17 \le k \le 10$, $-17 \le l \le 17$
Reflections collected/unique	12 174/4852 [*R*(int) = 0.200]	23 434/8265 [*R*(int) = 0.1044]	15 152/7511 [*R*(int) = 0.0326]
Completeness to theta = 26.37	99.8%	99.7%	99.7%
Absorption correction	Analytical	Analytical	Analytical
Max. and min. transmission	0.9802 and 0.8948	0.9430 and 0.8341	0.9250 and 0.8242
Refinement method	Full-matrix least-squares on F^2	Full-matrix least-squares on F^2	Full-matrix least-squares on F^2
Data/restraints/parameters	4852/134/432	8265/41/591	7511/14/506
Goodness-of-fit on F^2	0.822	1.026	1.054
Final *R* indices [$I > 2\sigma(I)$]	R_1 = 0.0769 wR_2 = 0.0771	R_1 = 0.0749 wR_2 = 0.1736	R_1 = 0.0396 wR_2 = 0.0982
R indices (all data)	R_1 = 0.1888 wR_2 = 0.0969	R_1 = 0.1408 R_2 = 0.2199	R_1 = 0.0524 wR_2 = 0.1060
Largest diff. peak and hole	0.370 and −0.392 e A^{-3}	1.127 and −0.572 e. A^{-3}	0.471 and −0.458 e A^{-3}

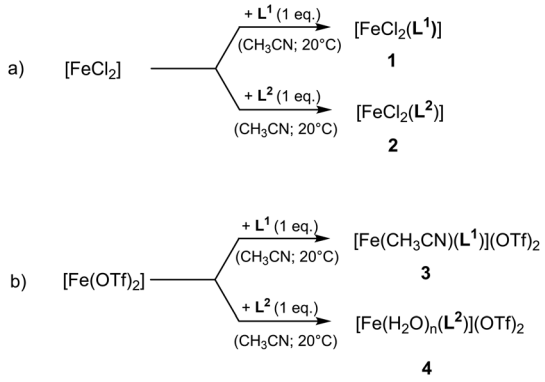

Scheme 1 Syntheses of the complexes reported in this study.

synthesized by stirring a mixture of $[Fe(OTf)_2]$ and the appropriate stoichiometric amount of $\mathbf{L^1}$ or $\mathbf{L^2}$ at room temperature (Scheme 1(b)). The syntheses and reaction conditions are outlined in Scheme 1.

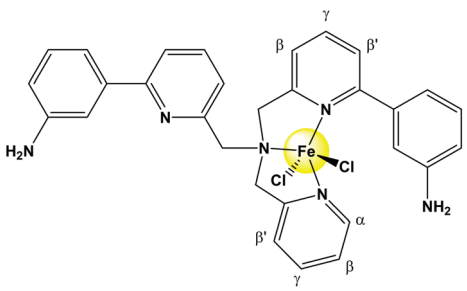

Chart 2 Proposed structure of complex **1**.

Characterization and studies of complexes 1–4

In most of the complexes obtained by the reaction of iron(II) salts (Cl^- or $SO_3CF_3^-$) with TPA derivatives, the metal centre adopts a distorted octahedral geometry, where the tripod coordinated in the κ^4 mode.[40,44,47,48,58,64–69] In contrast, only a few number of complexes display a distorted trigonal–bipyramidal geometry,[40,41,44,48,49] and moreover much fewer examples, where the metal is in a square-pyramidal environment, are known.[42,43,46]

Characterization of "$FeCl_2$" complexes 1 and 2

$[FeCl_2(L^1)]$ (1). We have not been able to isolate crystals suitable for an X-ray diffraction analysis, therefore the structure of **1**, shown in Chart 2, is based on spectroscopic data only. The structure of **1** was proposed by comparing its ^{1}H NMR pattern (see Table 2) with that of the already known complex $[FeCl_2(\mathbf{L^a})]$ ($\mathbf{L^a}$ = Ph_2TPA) (see Chart 1 for the ligand structure), for which the molecular structure has been well established by crystallography.[40] The main features in this structure are the tridentate coordination mode of the ligand $\mathbf{L^1}$, with one substituted pyridine remaining out of the coordination sphere, and the pentacoordination of the iron atom which lies in a distorted trigonal–bipyramidal environment. The ^{1}H NMR spectrum of **1** reflects a high-spin state for the metal with broad signals. For example, a very broad signal, attributable to the α proton of a coordinated pyridine, appears at 119.2 ppm. Three signals corresponding to the two protons each are observed at δ = 86.1, 32.2 and 17.3 ppm, and are assigned to the methylene groups (Table 2). Two other sharp resonances and two broad signals are found at 53.8 and 21.2, and 7.3 and 3.9 ppm. They may correspond to the β, β′ and γ protons of the coordinated pyridine, by analogy with similar Fe-TPA complexes.[40]

Table 2 ^{1}H NMR chemical shifts (δ, ppm) from complexes **1–4**, $[FeCl_2(\mathbf{L^a})]$ and $[FeCl_2(\mathbf{L^b})]$ in CD_3CN

	1[a]	**2**	**3**	**4**	$[FeCl_2(\mathbf{L^a})]$[g]	$[FeCl_2(\mathbf{L^b})]$[g]
CH$_\alpha$ (Py)	119.2[b,c]	102.2[b,c]	120.1[b,c]		120.0[b,d]	119.0[b,d]
CH$_2$	86.1[b,d]	53.7[b,c]	61.4[b,d]	38.2[b,d]	88.0[b,d]	62.0[b,d]
	32.2[b,d]	38.4[b,c]	59.1[b,d]	33.0[b,d]	31.0[b,d]	55.0[b,d]
	17.3[b,d]	33.3[b,d]	−9.8[b]	11.7[b,d]	21.0[b,d]	31.0[b,d]
CH$_{\beta,\beta'}$ (Py)	53.8[b]	45.7[b]	60.7[b]	62.4[b,c]	54.1[b]	51.1[b]
	51.2[b]	42.4[b]	46.5[b]	46.9[b,c]	52.9[b]	44.4[b]
		29.9[b]		30.5[b,c]		23.3[b]
CH$_\gamma$ (Py)	7.3[b,c]	11.7[b]	20.6[b,d]	9.2[b,d]	7.5[b,d]	13.1[b]
	3.9[b,d]	3.9[b]		8.7[b,d]	4.5[b,d]	11.0[b]
CH (not coord.)	0.57[b,d]	2.7[b]		1.28[b,d]	2.1[b]	
		0.35[b]		−0.32[b,d]	1.8[b]	
		−2.7[b,d]				
CH (subst. Ph)	10.0[b,d]	7.9[e]	11.5[b]	10.8[b,d]	10.8[b]	
	6.4[b,d]		7.3[b,d]	8.3[b,d]	7.0 [b]	
	1.5(+H_2O)[d]		5.4[b]	8.0–7.5[e]	4.8[b]	
				7.2[b,d]		
				3.9[b,d]		
NH$_2$	1.3[b]		−12.0[b]			
	1.1[b,d]					
NH		−8.7[b,d]		−2.86[b,d]		
OH (H_2O)				2.1[f]		

[a] Data in CD_2Cl_2. [b] Singlet. [c] Very broad. [d] Broad. [e] Multiplet. [f] Obscured. [g] Ref. 40.

The diamagnetic region of the spectrum displays on the one hand three broad peaks at 10.0, 6.4, and 1.5 (with water) ppm that are assigned to eight protons of two phenyl substituents, and on the other hand two singlets at 1.3, and 1.1 ppm that are attributed to two amine (NH_2) groups. There remains in the diamagnetic region one broad resonance at 0.57 ppm, corresponding to three protons, which are due to the uncoordinated pyridine. The formulation of **1**, proposed on the basis of ^{1}H NMR results, was confirmed by the ESI-MS spectrum, where the molecular peak was detected at 677.10 (calculated: 677.12). UV-visible spectroscopy of the complex in acetonitrile displayed two main absorption bands in the 250–300 nm wavelength range, and a less intense absorption band at 324 nm (Table 3). These three bands are consistent with the previous results obtained with analogous TPA complexes, such as [$FeCl_2$($\mathbf{L^a}$)].[40] It should be noted that the use of a TPA ligand having two pyridyl groups substituted each by a phenylamine moiety does not modify the mode of coordination of such a ligand towards a "$FeCl_2$" core, compared to that observed with the Ph_2-TPA ligand.[40]

[$FeCl_2$($\mathbf{L^2}$)] (2). The reaction of $FeCl_2$ with a macrocyclic ligand, namely $\mathbf{L^2}$ (see Chart 1) containing two different coordination sites for Fe^{2+}, has given in good yield a yellow-brown solid **2**. The analytical data of this solid indicate that **2** was formed with 1.5 molecules of water, and therefore was formulated as [$FeCl_2$($\mathbf{L^2}$)]·1.5H_2O. This formulation was confirmed by X-ray diffraction of a single crystal (see ORTEP in Fig. 1), obtained at room temperature by slow diffusion of diethyl ether in a dichloromethane solution of **2** with, however, the loss of H_2O. Selected bond lengths and angles for **2** are given in the caption of Fig. 1. The structural analysis of **2** reveals (i) the tridentate coordination mode of the ligand *via* its TPA arm, with one substituted pyridine remaining out of the coordination sphere that is completed by two chlorides and (ii) a distorted pentagonal geometry, for which the Addison index is equal to τ = 0.39, *i.e.* a value indicative of a noticeable distortion with respect to either the ideal trigonal–bipyramidal environment (τ = 1) or the square-pyramidal one (τ = 0).[70]

The small angles N7–Fe1–N1 (77.5(3)°) and N7–Fe1–N2 (76.9(3)°) reflect the high distortion observed in this geometry that is, however, closer to a square-pyramid than a trigonal-pyramid. The Fe^{II}–N distances, ranging from 2.130(2) to 2.259(2) Å, and Fe–Cl (~2.323 Å) are consistent with a high spin for the metal centre in **2** (see Fig. 1, caption).[43] As shown in Fig. 1, the long Cl1–H distances, *e.g.* Cl1–HN3 and Cl1–HN5, suggest at the most very weak interactions between these atoms. This indicates that the macrocyclic ligand $\mathbf{L^2}$ has a large cavity, which can explain why the PydCA (pyridine–dicarboxamide) arm does not coordinate to the "$FeCl_2$" core in **2**. The molecular conductivity measurement of a 1.5 mM solu-

Table 3 UV-Vis spectroscopic data (λ_{max} (nm) [ε_{max} (M^{-1} cm^{-1})]) for **1**, **2**, **3** and **4** and analogous complexes in CH_3CN at room temperature

Complex	λ_{max} (nm) [ε_{max} (M^{-1} cm^{-1})]		Λ/S cm^2 mol^{-1}	Ref.
1	257 [18 550], 285 [14 500]	324 [8160]	—	This work
2	253 [10 500]	341[3280], 386 [1785]	24	This work
3	259 [16 300], 283 [13 360]	335 [4880]	—	This work
4	253 [18 100], 284 [18 600]	—	138	This work
[$FeCl_2$(TPA)]	256 [8350]	427 [1440]	30	40
[$FeCl_2$($\mathbf{L^a}$)]	246 [17 900], 283 [17 030]	387 [6500]	28	40
[$FeCl_2$(MeTPA)]	258 [8860]	411 [1320]	36	44
[$FeCl_2$(Me_2TPA)]	261 [8770]	390 [900]	49	44
[$FeCl_2$(Me_3TPA)]	265 [6090]	371 [460]	42	44
[$FeCl_2$(Br_1TPA)]	261 [7520]	403.5 [1030]	30	40
[$FeCl_2$($\mathbf{L^b}$)]	262.5 [sh], 269 [10 430]	373 [620]	32	40
[Fe(FTPA)]	—	415 [1500]	31	45
[$FeCl_2$(F_2TPA)]	—	390 [1400]	36	45
[$FeCl_2$(F_3TPA)]	261 [8050]	—	41	41
[$FeCl_2$(ClTPA)]	259 [8300]	392 [1200]	—	49
[$FeCl_2$(Cl_2TPA)]	267 [9400]	373 [600]	—	49
[$FeCl_2$(Cl_3TPA)]	269 [13 300]	—	—	49
[FeL_2(ClTPA)](OTf)$_2$[a]	258 [10 200]	354 [1300]	—	49
[FeL_2(Cl_2TPA)](OTf)$_2$[a]	264 [8500]	351 [600]	—	49
[FeL_2(Cl_3TPA)](OTf)$_2$[a]	268 [9400]	344 [600]	—	49
[$FeCl_2$(^{OMe_2}PhTPA)]	258 [12 326], 280 [8268]	376 [1015]	46	46
[$FeCl_2$(^{OMe_2}Ph_2TPA)]	251 [sh], 284 [14 735]	368 [752]	47	46
[$FeCl_2$(^{OMe_2}Ph_3TPA)]	247 [sh], 278 [19 003]	—	23	46
[$FeCl_2$(PivTPA)]	—	419 [840]	11	47
[$FeCl_2$(Piv_2TPA)]	—	379 [960]	6	47
[$FeCl_2$(RCO_2TPA)]	—	400 [740]	20	47
[$FeCl_2$(ITPA)]	258 [5500]	375 [1000]	19	48
[$FeCl_2$(I_2TPA)]	246 [7100]	370 [500]	23	48
[$FeCl_2$(I_3TPA)]	—	—	15	48
[$FeCl_2$(α-CN_2TPA)]	—	462 [800]	21	69
[$FeCl_2$(α-$CONH_2$TPA)]	—	368 [1300], 505 [1660]	—	69

[a] L = CH_3CN.

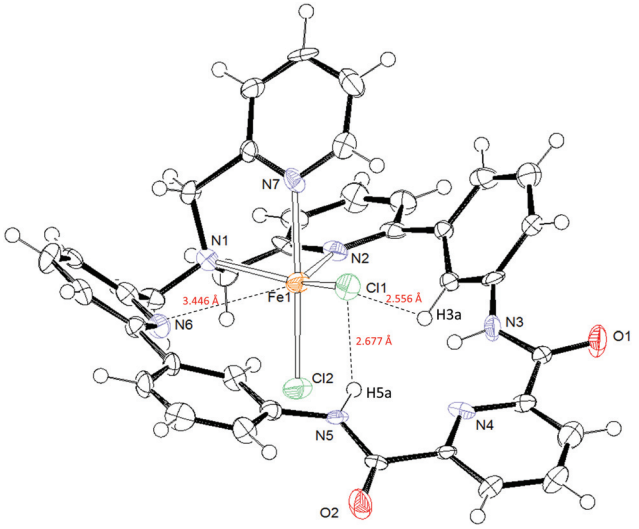

Fig. 1 ORTEP diagram of $[FeCl_2(L^2)]$ (**2**). Here and elsewhere non-hydrogen atoms are shown with 50% ellipsoids. Selected bond distances (Å) and angles (°): N1–Fe1 = 2.240(7), N2–Fe1 = 2.299(8), N7–Fe1 = 2.154(8), Fe1–Cl1 = 2.308(3), Fe1–Cl2 = 2.366(3), N7–Fe1–N1 = 77.5(3), N7–Fe1–N2 = 76.9(3), N1–Fe1–N2 = 78.2(3), N7–Fe1–Cl2 = 167.9(2), N1–Fe1–Cl2 = 94.5(2), N2–Fe1–Cl2 = 92.8(2), N7–Fe1–Cl1 = 90.1(2), N1–Fe1–Cl1 = 144.70(19), N2–Fe1–Cl1 = 131.4(2), Cl2–Fe1–Cl1 = 101.54(10).

tion of **2** in acetonitrile yielded Λ = 24 S cm^2 mol^{-1}, indicating a neutral electrolytic behaviour of the compound in solution at this concentration,[71,72] and this implies that the solvent (CH_3CN) has not displaced any chloride ligand from the coordination sphere. The ^{1}H NMR spectrum of **2** in CD_3CN exhibits numerous well-defined paramagnetically shifted signals over the 103 to 53 ppm range, which confirms the high-spin state of the iron atom in the complex (see Table 2). All these data converge towards retention of the solid state structure when the compounds are dissolved in CH_3CN or CD_3CN.

Voltammetric studies of complex **2** were carried out under an inert atmosphere in dichloromethane (DCM) and acetonitrile (MeCN) with NBu_4PF_6 as the supporting electrolyte. In DCM, complex **2** displayed an irreversible oxidation peak in a cyclic voltammogram (CV) at $E_{pa}(1)$ = 0.33 V *vs.* Fc at v = 0.1 V s^{-1} (Fig. 2) when scanning toward positive potential values.

On the back scan, a reduction peak was detected at $E_{pc}(2)$ = −0.50 V. The latter peak was not present when the scan was processed in the negative direction. Variation of the scan rate did not modify the redox behavior. Rotating-disk Electrode Voltammetry (RDEV) showed an oxidation wave at $E_{1/2}$ = 0.30 V *vs.* Fc (Fig. 2). Exhaustive electrolysis of the solution at 0.5 V suggested a monoelectronic oxidation process from coulometric measurements. RDEV after electrolysis displayed a unique reduction wave at −0.50 V. Reduction of the electrochemically generated species yielded back the initial complex **2**. In acetonitrile, the same

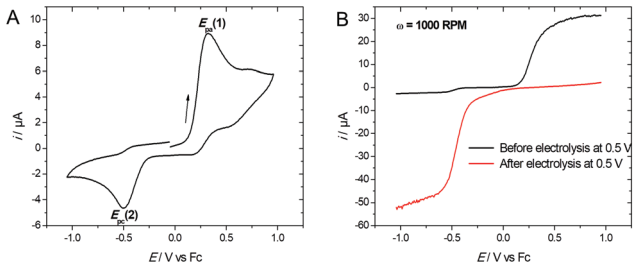

Fig. 2 (A) CV (*E*/*V vs.* Fc) at a Pt working electrode of **2** (1 mM) in CH_2Cl_2/NBu_4PF_6 0.1 M (v = 0.1 v s^{-1}); (B) RDEV before (black) and after (red) exhaustive electrolysis at 0.5 V *vs.* Fc (ω = 1000 RPM).

behaviour was observed, except for a slight difference in redox potential values which can be ascribed to the higher polarity of the medium.

Hence, these results suggest that the monoelectronic oxidation of complex **2** at $E_{pa}(1)$ is followed by a chemical reaction, leading to a new species which can be reduced at $E_{pc}(2)$. The large peak-to-peak separation (800 mV) indicates a strong rearrangement of the coordination sphere upon electron exchange. This can be considered in the frame of a square-scheme mechanism, as often found for coordination metal complexes.[73] Here, the oxidation of **2** leads probably to the formation of a transient pentacoordinated $[Fe^{III}Cl_2(\mathbf{L}^2)]^+$ species, which evolves toward a more stable hexacoordinated complex $[Fe^{III}Cl_2(\mathbf{L}^5)(Solv)]^+$ by incorporation of a solvent in the coordination sphere (Solv = H_2O, CH_3CN) (Scheme 2). The binding of a pyridyl moiety to the iron(III) centre is unlikely due to the rigidity of the ligand.

In contrast, the reduction of this species yields back the initial complex **2** by solvent release. For comparison with similar complexes, electrochemical data in acetonitrile are gathered in Table 4. Noticeably, the oxidation potential of complex **2** (0.26 V *vs.* Fc) in acetonitrile is significantly much higher than that reported for analogous complexes. If one assumes that the metal ion is penta-coordinated including two chloride ions, this high potential value can be ascribed to the ligand topology which disfavours the stabilization of the metal ion in a high redox state (here Fe^{III}) by the electrolyte. Such an effect was previously observed for analogous copper complexes.[74,75]

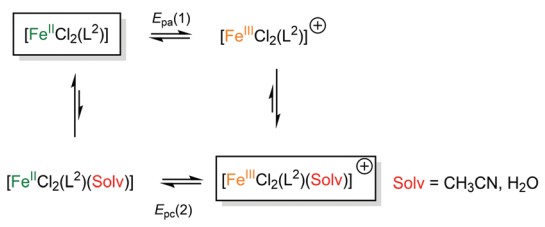

Scheme 2 Square scheme proposed for the redox behaviour of complex **2**.

Table 4 Electrochemical data (E/V *vs.* Fc, v = 0.1 V s^{-1}) for complex **2** in CH_3CN compared to those obtained for complexes $[FeCl_2(L^a)]$, $[FeCl_2(TPA)]$, $[FeCl_2(Me_1TPA)]$, $[FeCl_2(Me_2TPA)]$, $[FeCl_2(Me_3TPA)]$, $[FeCl_2(^{OMe_2}PhTPA)]$, $[FeCl_2(^{OMe_2}Ph_2TPA)]$ and $[FeCl_2(^{OMe_2}Ph_3TPA)]$

Complex	E_{pa}	E_{pc}
2	0.26[a]	−0.38[a]
$[FeCl_2(\mathbf{L^a})]$[b]	0.13	−0.39
$[FeCl_2(TPA)]$[b]	−0.15	−0.23
$[FeCl_2(Me_1TPA)]$[b]	−0.10	−0.19
$[FeCl_2(Me_2TPA)]$[b]	0.03	−0.08
$[FeCl_2(Me_3TPA)]$[b]	0.16	0.03
$[FeCl_2(^{OMe_2}PhTPA)]$[c]	−0.15	−0.24
$[FeCl_2(^{OMe_2}Ph_2TPA)]$[c]	−0.33	−0.41
$[FeCl_2(^{OMe_2}Ph_3TPA)]$[c]	0.00	−0.08

[a] Irreversible peak. [b] Ref. 44. [c] Ref. 46.

Characterization of "$Fe(OTf)_2$" complexes 3 and 4

$[Fe(CH_3CN)(L^1)](OTf)_2$ (3). The reaction of $Fe(OTf)_2$ with $\mathbf{L^1}$ in CH_3CN gave a red-orange solid **3**, in valuable yield (Scheme 1b). Formulation of **3** is based on the X-ray analysis of a single crystal of the complex obtained by slow diffusion of Et_2O into a CH_3CN solution of the product in a sealed tube. The molecular structure of **3** (see Fig. 3) shows that the complex is an ionic species, with a pentagonal dication in which the tripodal ligand $(PhNH_2)_2TPA$ coordinates in the tetradentate fashion, the coordination sphere being completed by a CH_3CN molecule. Two triflate anions ensure the neutrality of the compound. The main features in this structure are (i) the metal centre lying in a distorted pentagonal environment and (ii) an Addison index of 0.5, indicating that the geometry is equally distant between a square-pyramid and a trigonal-pyramid. The acute angles N5–Fe–N1, N6–Fe–N1, and N2–Fe–N1 (~75.86(6)°) confirm the high distortion observed in this geometry (Fig. 3 caption). In **3**, all the Fe^{II}–N distances, ranging from 2.116(2) to 2.215(2) Å, are typical of a high spin for the metal centre. Therefore, the crystallographic data clearly indicate that the two triflate ligands in $Fe(OTf)_2$ are both displaced from the coordination sphere of the metal when this complex reacted with the disubstituted-TPA $\mathbf{L^1}$ ligand in a good coordinating solvent, such as CH_3CN. It should be noted that in the cation of **3**, the nitrogen atoms of the two NH_2Ph-substituted pyridine groups of the tertiary amine are bound to the iron centre, which notably differs from what was observed in an analogous neutral compound previously obtained by treating $FeCl_2$ with Ph_2-TPA in which one of the substituted pyridines is not bound to the metal.[40] Obviously, $[Fe(CH_3CN)(\mathbf{L^1})]$ $(OTf)_2$ (**3**) can be compared with the already known six-coordinate complex $[Fe(CH_3CN)_2(TPA)](OTf)_2$,[64] both were obtained under very similar conditions. Both ligands, $\mathbf{L^1}$ and TPA, act as tetradentates in **3** as well as in the bis-nitrile derivative. But, in the latter, the metal centre lies in a nearly standard octahedral "N6" environment with Fe–N distances of 1.934(3)–1.978(3) Å,[64] which are typical of low-spin iron(II),[76] whereas in **3**, the iron atom lies in a distorted pentagonal "N5" geometry with characteristic Fe–N distances of a high-spin Fe(II) (see above). Another obvious difference in these structures lies in the values of the Fe–N–C(CH_3) angles, which are nearly linear in the bis-nitrile compound (175°),[64] whereas the distortion from linearity becomes more marked in **3** (171.11(19)°). These differences are probably due to steric factors, which are more pronounced in **3** than in the bis-nitrile complex. The ^{19}F NMR spectrum of **3** in CD_3CN solution exhibits only one resonance at δ = −78.2 ppm (see the Experimental section), in line with the presence of free triflate ions,[77] indicating that the structure of the complex as seen in the solid state is retained in solution. The ^1H NMR spectrum displays some paramagnetically shifted and broad resonances within the 120–20 ppm range, thus confirming the high-spin state of the metal as deduced from the crystal structure analysis of the solid. The ^1H NMR pattern of **3** presents some similarities and also some differences with those of other distorted (albeit more or less distorted) trigonal–bipyramidal derivatives, such as complexes **1**, **2**, $[FeCl_2(\mathbf{L^a})]$ and $[FeCl_2(\mathbf{L^b})]$ (see Table 2). Differences between the patterns of these five complexes are due mainly to TPA ligands that have varied pyridine substituents, and as a result different distortion degrees of these geometries relative to the ideal trigonal-bipyramid. In spite of some differences, the ^1H NMR resonances of **3** have been attributed as indicated in Table 2 by comparison with those of the distorted pentagonal complexes **1**, **2**, $[FeCl_2(\mathbf{L^a})]$ and $[FeCl_2(\mathbf{L^b})]$.

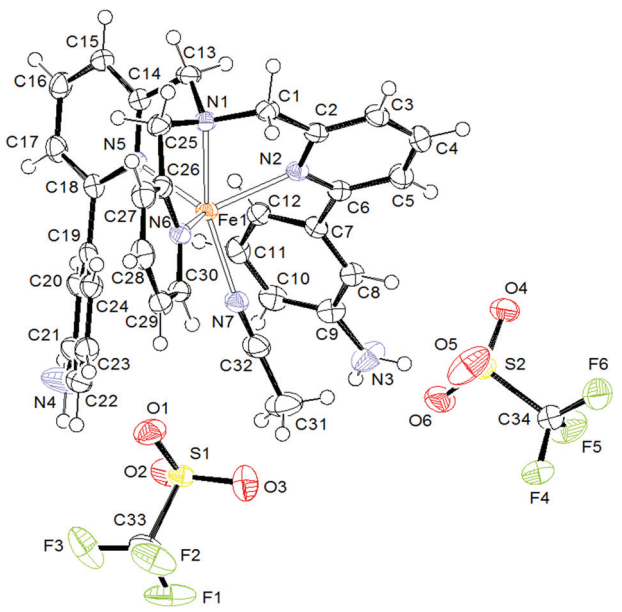

Fig. 3 ORTEP diagram of $[Fe(CH_3CN)(L^1)](OTf)_2$ (**3**). Selected bond distances (Å) and angles (°): N1–Fe1 = 2.2147(17), N2–Fe1 = 2.1819(18), N5–Fe1 = 2.126(18), N6–Fe1 = 2.1555(18), N7–Fe1 = 2.1159(19), N7–Fe1–N5 = 126.54(7), N7–Fe1–N6 = 93.04(7), N5–Fe1–N6 = 111.77(7), N7–Fe1–N2 = 93.55, N5–Fe1–N2 = 111.66(7), N6–Fe1–N2 = 119.17(6), N7–Fe1–N1 = 156.83(7), N5–Fe1–N1 = 76.63(7), N6–Fe1–N1 = 76.07(6), N2–Fe1–N1 = 74.89(6), C32–N7–Fe1 = 171.11(19).

$[Fe(H_2O)_n(L^2)](OTf)_2$ (4) (n = 1 or 2). Complex **4** was obtained in moderate yield, as a red-orange solid by reacting $Fe(OTf)_2$ with the macrocyclic ligand $\mathbf{L^2}$. Unfortunately, we have not been able to isolate crystals of this product suitable for an X-ray diffraction analysis. Therefore, the structure of **4** is based on mass, molar conductance and spectroscopic data. The higher peak observed in the mass spectrum at m/z = 880.2, corresponding to $\{Fe(OTf)(H_2O)_4(\mathbf{L^2})\}^+$, can be explained by the presence of traces of water in the solvent (CH_3CN). The presence of H_2O in **4** is confirmed by resonance at 2.1 ppm in the ^{1}H NMR spectrum (Table 2). The molar conductivity, Λ = 138 S cm^2 mol^{-1}, was measured in CH_3CN and its value indicates an ionic behaviour in solution. No resonance attributable to a coordinated triflate was observed in the ^{19}F NMR (CD_3CN) spectrum, and only one species was present. The chemical shift, δ = −79.6 ppm, corresponds to free triflate ions. This datum suggests for **4** a dicationic species in spite of the relatively low value of the molar conductance (see above), which is more characteristic of a singly-charged species than a doubly one.[40,65] Nevertheless, on the basis of these data, we suggest for **4** either the pentagonal $[Fe(H_2O)(\mathbf{L^2})](OTf)_2{\cdot}3H_2O$ geometry or the octahedral $[Fe(H_2O)_2(\mathbf{L^2})](OTf)_2{\cdot}2H_2O$ one. Unhappily, ^{1}H NMR (Table 2) and UV-visible (Table 3) spectroscopies do not allow one to distinguish unquestionably between these two possibilities.

Reactivity of complexes 1–4 towards H_2O_2

The reactivity of iron complexes towards H_2O_2 was investigated in acetonitrile at room temperature by using UV-Vis and EPR spectroscopy to monitor the reaction. Addition of hydroperoxide (0.5 to 35 molar eq.) to a solution of complex **1** led to the appearance of two absorption bands at λ_{max} = 360 nm (ε = 9780 M^{-1} cm^{-1}) and 314 nm (ε = 6670 M^{-1} cm^{-1}). The presence of an isosbestic point at λ_{max} = 336 nm for 15 eq. indicated that no secondary reaction occurred (see the ESI‡). The spectrum did not evolve after the addition of 35 molar eq. Moreover, the EPR spectrum of complex **1** after the addition of H_2O_2 in excess displayed an intense and broad signal at g = 4.25. According to previous results, these spectroscopic data suggest the formation of high-spin mononuclear Fe^{III}–O_2 adducts or dinuclear (μ-oxo) bis-iron(III) species.[78]

Different results were obtained for the macrocyclic complexes **2** and **4**. Hence, the addition of hydrogen peroxide (25 eq.) at 293 K induced the formation of two absorption bands at λ_{max} = 357 nm and 555 nm for **2**, as well as 362 nm and 587 nm for **4** (Fig. 4). In both cases, the monitoring of the absorbance for these two new bands indicated a relatively fast (20 min) process at room temperature, and a rather slow evolution of the formed species (>2 h) (see for example Fig. 4 for complex **2**, inset). According to literature data, these spectroscopic features can be ascribed to either hydroperoxo Fe^{III}(OOH) or Fe^{III}(OH) hydroxo species.[49,69,79,80] Indeed, these species classically display a hydroperoxo or hydroxo to Fe^{III} charge transfer (LMCT) in the 310–360 and 500–600 nm wavelength ranges (ε = 3600–5300, and 1000–2000 M^{-1} cm^{-1}, respectively). Also, phenolate Fe^{III} complexes exhibit absorption bands in this wavelength range.[29]

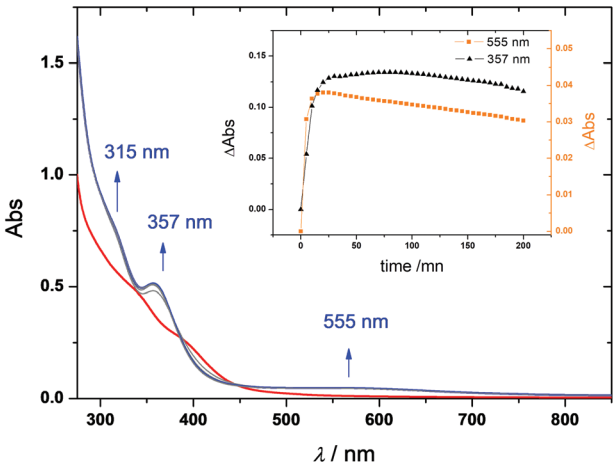

Fig. 4 UV-Vis spectra of **2** (1.4 mM) in CH_3CN (red) and after (blue) the addition of 35 molar eq. of H_2O_2. Inset: monitoring of the absorbance *vs.* time at λ_{max} = 555 nm (black triangles) and λ_{max} = 357 nm (orange squares).

It should be noted that any tentative attempt to make complex **2** react with O_2 failed, when dioxygen was bubbled through a CH_3CN solution of **2** (under UV-visible monitoring). Therefore, stronger oxidants than O_2 are required for oxidizing this di-iron compound. For this, compound **4** was reacted with 10 eq. of H_2O_2 in CH_3CN (Scheme 3). As mentioned above, after stirring and required treatments, small amounts of a red-orange powder, **2′**, were isolated. In order to better understand this process, the product was analyzed. The UV-visible spectrum of **2′** in CH_3CN displays a pattern close to that described for **2** (see Fig. 4). Crystals of **2′** suitable for an X-ray study have been obtained (see the Experimental part). Compound **2′**, which was isolated in low yields, was characterized only in the solid state by crystallography. X-ray diffraction analysis (Fig. 5) revealed that the ionic complex $[\{Fe(O\mathbf{L^{2'}})\}_2(\mu\text{-}OH)_2]^{2+}[(FeCl_3)_2(\mu\text{-}O)]^{2+}{\cdot}3CH_3CN$ (**2′**), where $\mathbf{L^{2'}}$ = $\mathbf{L^2}$–$1H_{Ph}$, was formed. In the symmetric bis(μ-hydroxo)diiron(III) dication, the $O\mathbf{L^{2'}}$ ligands are coordinated *trans* to each other in the hypodentate fashion. Each iron centre adopts a distorted octahedral geometry, and the tripod coordinates in the κ^4-(N,O) mode, by involving three nitrogen atoms, N1, N2 and N3, and one oxygen (O3) of a phenoxo group. Two oxygen atoms of hydroxo groups complete the coordination sphere of iron atoms by sharing the two octahedra. All Fe–N distances are longer than 2.1 Å (see Fig. 5, caption) and lie in the expected range for high-spin ferric derivatives.[81] The N1 and

$$[FeCl_2(\mathbf{L^2})] + H_2O_2 \xrightarrow{CH_3CN} [\{Fe^{III}(\mu\text{-}OH)(O\mathbf{L^{2'}})\}_2][FeCl_3)_2(\mu\text{-}O)], 3\,H_2O$$

2 **2′**

Scheme 3 Formation of complex **2′**.

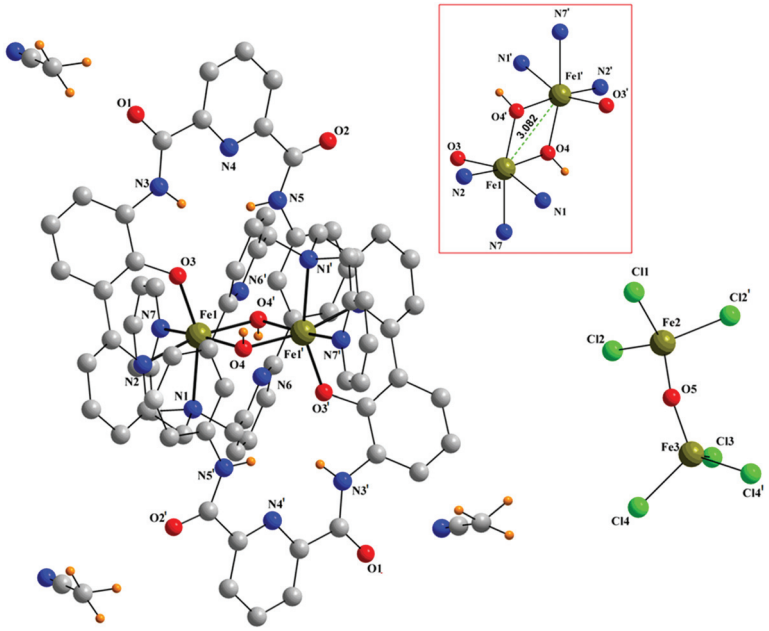

Fig. 5 "Ball and stick" model of complex **2′**, $[\{Fe(OL^{2'})\}_2(\mu\text{-}OH)_2]^{2+}[(FeCl_3)_2(\mu\text{-}O)]^{2+}\cdot 3CH_3CN$, showing the atom labelling scheme. Thermal ellipsoids are plotted at 10% probability. Hydrogen atoms have been omitted for clarity (except for the hydroxido ones). Selected bond distances (Å) and angles (°) in the dication: Fe1–Fe1′ = 3.082(5), Fe1–N1 = 2.241(5), Fe1–N2 = 2.142(4), Fe1–N7 = 2.170(4), Fe1–O3 = 1.886(4), Fe1–O4 = 1.955(4), Fe1–O4′ = 2.022(4), N3–H3N = 0.869(18), N5–H5N = 0.856(12), O4–H4w = 0.830(2), N1–Fe1–N2 = 75.96(17), N1–Fe1–N7 = 76.65(17), N1–Fe1–O3 = 157.35(17), N2–Fe1–N7 = 97.20(17), N2–Fe1–O3 = 88.13(17), N7–Fe1–O3 = 89.73(17), N7–Fe1–O4 = 93.30(16), N7–Fe1–O4′ = 168.63(15), N1–Fe1–O4 = 98.20(16), N1–Fe1–O4′ = 96.66(16), N2–Fe1–O4 = 166.38(17), N2–Fe1–O4′ = 89.95(16), O3–Fe1–O4 = 100.60(16), O3–Fe1–O4′ = 99.37(15), Fe1–O4–Fe1′ = 101.60(15), Fe1–O4–H4w = 103.00(4), Fe1′–O4–H4w = 121.00(4). Selected bond distances (Å) and angles (°) in the dianion: Fe2–O5 = 1.790(6), Fe2–Cl = 2.233(2), Fe3–O5 = 1.754(5), Fe3–Cl3 = 2.225, Fe–Cl4/4′ = 2.204(4), Fe2–O5–Fe3 = 140.40(3), Cl1–Fe2–Cl2 = 109.21(6), Cl1–Fe2–Cl2′ = 109.21(6), Cl1–Fe2–O5 = 110.61(10), Cl2–Fe2–Cl2′ = 108.59(9), Cl3–Fe3–Cl4 = 110.14(7), Cl3–Fe3–Cl4′ = 110.14(7), Cl4–Fe–Cl4′ = 104.18(13), Cl3–Fe3–O5 = 107.80(19), Cl4–Fe3–O5 = 112.29(12), Cl4′–Fe3–O5 = 112.29(12).

O3 atoms on one hand, and the O3′ and N1′ atoms on the other hand occupy apical positions with N–Fe–O ~157°. Furthermore, the $Fe_2O_2(H)$ core in the dication of **2′** makes the angle O–Fe–O = 78.40(16)° more acute than the Cl–Fe–Cl = 101.54(10)° in the parent neutral compound **2**, then allowing a tetradentate coordination of the $OL^{2'}$ ligand. The iron–oxygen$_{(phenoxo)}$ distance, 1.8864(4) Å, suggests a relatively strong Fe1–O3 bond. Thus the oxidation of **2** by H_2O_2, leading to the formation of **2′**, implies the activation of one C–H bond of a phenyl group and the concomitant oxidation of the related ligand *via* the loss of a hydrogen, which is replaced by an oxygen atom. Usually, upon reaction of dichloroiron(II) species with molecular dioxygen, hydrogen peroxide or organic peroxides, μ-oxo dinuclear complexes are obtained.[82] Here, such a reaction gives rise to a bis-μ-hydroxo compound with an Fe–OH distance of 2.022 Å, which is comparable to that found in similar hexacoordinating iron(II/III) complexes.[78] The Fe1–O–Fe1′ angle (101.60(15)°) is close to that observed in this type of compound (~104.70°), as well as the Fe1–Fe1′ distance (3.082 Å) that is comparable to the values reported in the literature.[78] Such a distance is short and cannot exclude an interaction between the two iron atoms which differs from those found in μ-oxo diiron(II) complexes having TPA ligands (3.456–3.575 Å), where the two iron centres are formally non-bonded.[41,45,46,66,81,83] In the latter compounds the Fe–O–Fe angles are quite less acute (~166.4°) than that in the dication of **2′**. The dianion $[Fe(Cl_3)_2(\mu\text{-}O)]^{2+}$ is present in **2′** as the counter-ion. The dianion has already been reported in the literature as a counter-ion in the manganese(II)[84] and iron(II)[85] complexes, $[Mn(C_3H_7NO)][(FeCl_3)_2(\mu\text{-}O)]$, where C_3H_7NO = dimethylformamide, and $[Fe(1,10\text{-phen})_3][(FeCl_3)_2(\mu\text{-}O)]$. In all of these complexes, each iron(III) centre lies in a pseudo-tetrahedral environment. Recently, Tinberg and Lippard have shown that two hydroxide ligands bridge the iron atoms, which are separated by 3.1 Å, in the diiron(III) resting state of the enzyme (MMOHx).[17] Interestingly, the $\{Fe(\mu\text{-}OH)_2Fe\}$ core in the dication of **2′** displays similar geometrical data to those observed in this enzyme, with two bridging hydroxide ligands and a Fe^{III}–Fe^{III} distance equal to 3.082 Å (see Fig. 5).

Reactivity of complexes 1–4 towards *m*-CPBA

The reactivity of complex **3** towards *m*-CPBA was also investigated by UV-Vis spectroscopy at low and room temperatures in acetonitrile. Room temperature studies did not allow the characterization of any transient species, probably due the high rate of the reaction, as shown by the change of the colour of the solution (red to green). However, as shown in Fig. 6, the addition of an oxidant to a solution of **3** at −40 °C led to the formation of two new bands at λ_{max} = 709 nm (ε = 335 M^{-1} cm^{-1}) and 520 nm (ε = 610 M^{-1} cm^{-1}). While the former

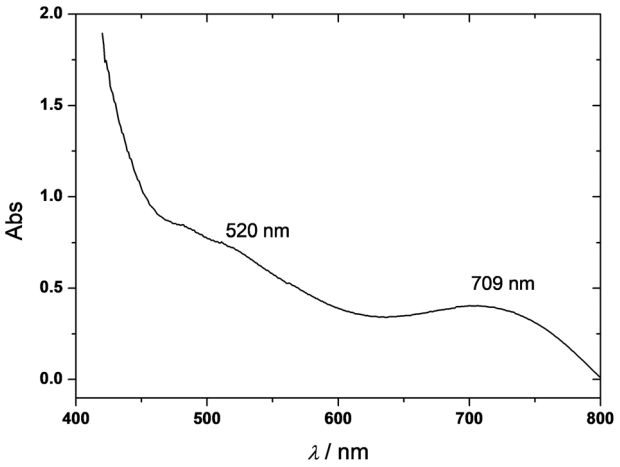

Fig. 6 UV-Vis spectrum of **3** (2.5 mM) in CH_3CN after the addition of 1.2 molar eq. of *m*-CPBA (optical path: 5 mm) at −40 °C.

decreased progressively with time ($t_{1/2}$ = 13 min), the latter kept on increasing to attain a steady state value. These results are reminiscent of that obtained for the analogous $[Fe^{II}(TPA)(CH_3CN)_2]^{2+}$ complex.[86] Indeed, a transient species was detected at λ_{max} = 724 nm ($\varepsilon \approx 300\ M^{-1}\ cm^{-1}$) upon addition of peracetic acid at low temperature (−40 °C). This absorption band was ascribed to a d–d transition within the $[Fe^{IV}(O)(TPA)]^{2+}$ complex. Similarly, the reaction of $[Fe^{II}(6\text{-MeTPA})(CH_3CN)_2]^{2+}$ with peracetic acid at low temperature yielded a new species which displayed an absorption band at λ_{max} = 770 nm ($\varepsilon \approx 300\ M^{-1}\ cm^{-1}$), ascribed to a Fe(IV)-oxo species.[87] Hence, these results suggest that the reaction of complex **3** with *m*-CPBA leads possibly to the transient species $[Fe^{IV}(O)(\mathbf{L^1})]^{2+}$, as shown in Scheme 4.

Comparative catalytic activity of 1–4 for cyclohexane oxidation

Catalytic oxidation of cyclohexane by H_2O_2. The reaction studies with H_2O_2 were performed by adding hydrogen peroxide (1 eq.) to a solution of cyclohexane (1 eq.) containing 0.001 eq. of iron(II) catalyst, as depicted in Scheme 5. The experiments were carried out first in the absence and then in the presence of acetic acid (AcOH, 0.5 eq.) in order to enhance the yield of the reaction. Indeed, AcOH is well known for inhibiting the decomposition of hydrogen peroxide into water and

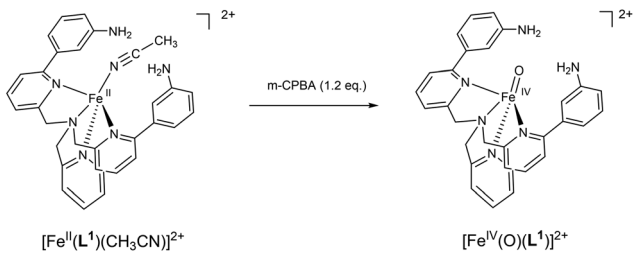

Scheme 4 Reactivity of complex **3** with *m*-CPBA, leading to the formation of $[Fe^{IV}(O)(\mathbf{L^1})]^{2+}$.

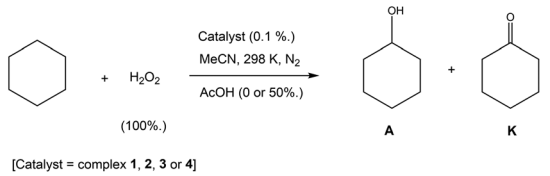

Scheme 5 Catalytic oxidation of cyclohexane by **1**, **2**, **3** or **4** in the presence of H_2O_2 with/without acetic acid (AcOH), leading to the formation of cyclohexanol (A) and cyclohexanone (K). Percentages indicate the molar equivalents *vs.* cyclohexane.

dioxygen. Moreover, it has been proposed that acetic acid could promote the heterolytic (*vs.* homolytic) cleavage of the O–O bond in Fe^{III}–hydroperoxo adducts, leading to reactive high-valent Fe^{V}-oxo species.[79,88]

Data obtained from GC analysis for the different catalysts **1–4** are gathered in Table 5. Considering the turnover number, [A]/[K] and yield values, it appears clearly that the topology of the TPA-based ligand, $\mathbf{L^1}$ or $\mathbf{L^2}$, significantly impacts the catalytic properties. As shown in Fig. 7, the yield and turnover numbers for the production of both A and K are more enhanced with complexes **2** and **4**, by *ca.* a three-fold factor, than with **1** and **3**. In particular, the TONs are greater (between 6 and 9) in the absence of acetic acid. The selective oxidation towards A or K species seems however poorly affected by the nature of the complex or by the concentration in AcOH.

Catalytic oxidation of cyclohexane by *m*-CPBA. The catalytic properties of complexes **1–4** were also investigated by using

Table 5 Data for the catalytic oxidation of cyclohexane by **1**, **2**, **3** or **4** in the presence of H_2O_2

Catalyst	AcOH (eq.)	TON (A)	TON (K)	TON (A) + TON (K)	[A]/[K]	Yield (%)
1	0	1.6	1.9	3.5	0.83	0.1
	0.5	0.3	0.4	0.7	0.74	<0.1
2	0	5.7	8.9	14.6	0.64	0.8
	0.5	2.9	3.6	6.5	0.80	0.4
3	0	0.5	0.4	0.9	1.29	<0.1
	0.5	0.5	0.4	0.9	1.10	<0.1
4	0	6.2	7.4	13.6	0.83	0.8
	0.5	0.3	0.3	0.6	1.00	<0.1

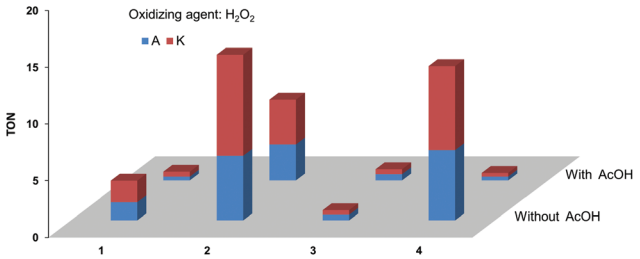

Fig. 7 Representative histogram for the turnover number for the catalytic oxidation of cyclohexane into cyclohexanol (A, blue) and cyclohexanone (K, red) by **1**, **2**, **3** or **4** in the presence of H_2O_2.

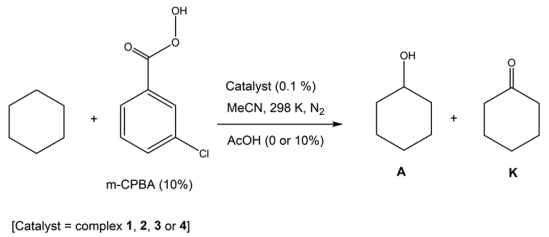

Scheme 6 Catalytic oxidation of cyclohexane by **1**, **2**, **3** or **4** in the presence of *m*-CPBA with/without acetic acid (AcOH), leading to the formation of cyclohexanol (A) and cyclohexanone (K). Percentages indicate the molar equivalents *vs.* cyclohexane.

m-CPBA as the oxidizing agent. As shown in Scheme 6, *m*-CPBA (0.1 eq.) was gently added to a solution of cyclohexane (1 eq.) containing an iron(II) catalyst (0.001 eq.). As for H_2O_2, the influence of AcOH (0.1 eq.) on the yield of the reaction was investigated.

Fig. 8 displays the turnover numbers obtained for the reaction yielding both A and K species. The best TON values were obtained for complexes **1** and **2** (see Table 6 for data), indicating that the presence of the chloride ligand significantly enhanced the oxidation reaction with this oxidizing agent. In particular, complex **2** reached *ca.* 30 TONs in the absence of AcOH. It should be noted that the selectivity (A *vs.* K) of the catalyzed reaction is higher than that observed with H_2O_2. Here, complex **2** displayed a remarkable 4.52 ratio for [A]/[K]

Fig. 8 Representative histogram for the total turnover number for the catalytic oxidation of cyclohexane into cyclohexanol (A, blue) and cyclohexanone (K, red) by **1**, **2**, **3** or **4** in the presence of *m*-CPBA.

Table 6 Data for the catalytic oxidation of cyclohexane by **1**, **2**, **3** or **4** in the presence of *m*-CPBA

Catalyst	AcOH (eq.)	TON (A)	TON (K)	TON (A) + TON (K)	[A]/[K]	Yield (%)
1	0	4.7	5.4	10.1	0.87	0.4
	0.5	10.4	3.9	14.3	2.66	0.6
2	0	24.4	5.4	29.8	4.52	1.8
	0.5	6.1	4.5	10.6	1.36	0.6
3	0	2.6	1.1	3.7	2.35	0.2
	0.5	3.1	1.7	4.8	1.84	0.2
4	0	1.7	0.5	2.2	3.40	0.1
	0.5	*a*	*a*	*a*	*a*	*a*

[a] No data available.

(Table 6), together with a relatively moderate reaction yield. This selectivity dropped to 1.36 when acetic acid was used as the co-factor.

Discussion on the coordination chemistry of complexes 1–4

Solid state and solution characterization has shown that the iron(II) ion is mainly pentacoordinated in the TPA core for all high-spin complexes **1**, **2**, **3** and **4**, whatever the nature of the counter-ion (Cl^- or OTf^-). The Fe^{II} centre is bound to the nitrogen atom of the tertiary amine and two N atoms of two different pyridyl groups (one substituted and one unsubstituted), the coordination sphere being completed by either one or two counter-ions, one or two molecules of solvent or the remaining substituted pyridyl group. The solid state structures obtained from X-ray diffraction analysis for **2** and **3** indicate a geometrical pattern in-between square-based pyramidal (SBP) and trigonal–bipyramidal (TBP), the TPA core being essentially coordinating in a tridentate fashion. More specifically, the macrocyclic complex **2** displays one free substituted pyridyl group, the structure being too rigid to accommodate the coordination of all N-atoms of the TPA system. To better account for the effect of the ligand topology, complexes **1–4** can be compared with their previously reported TPA and Ph_2TPA analogues.[40]

Solid state analysis of $[Fe^{II}Cl_2(TPA)]$ showed that the metal ion is hexacoordinated in a pseudo-octahedral geometry with two equatorial chloride ions (Scheme 7). The substitution of the H atom by phenyl groups on two of the three pyridyl moieties, leading to $[Fe^{II}Cl_2(\mathbf{L}^a)]$, induces a strong modification of the coordination sphere (Scheme 7). Indeed, X-ray diffraction analysis showed that the tripodal Ph_2TPA core coordinates in a tridentate mode in the presence of chloride ions, because of steric repulsion, as observed in other α-disubstituted TPA complexes.[40] In addition, the geometry around the Fe(II) centre is no longer pseudo-octahedral but rather trigonal bipyramidal. These coordination features are conserved in acetonitrile. Hence, on the basis of NMR, UV-Vis and conductivity measurements, complexes **1** and **2** display similar structural properties to $[Fe^{II}Cl_2(\mathbf{L}^a)]^{2+}$ in acetonitrile, the iron(II) centre being pentacoordinated as depicted in Scheme 7.

As for its bis-chloride analogue, $[Fe^{II}(TPA)(CH_3CN)_2]^{2+}$ is characterized in the solid state by an octahedral geometry around the ferrous centre (Scheme 7), the two nitrile ligands being coordinated in the *cis*-position.[89] These structural features are maintained even when the solid is dissolved in acetonitrile. When the TPA core is substituted by the 6-Me_3TPA ligand, the resulting complex, $[Fe^{II}(6\text{-}Me_3TPA)(CH_3CN)_2]^{2+}$, displays also a 6-coordinated pseudo-octahedral structure thus indicating that the methyl substituting groups do not induce significant steric constraints (Scheme 7).[89] The same conclusion was obtained with the more sterically-hindered complex $[Fe^{II}(BQPA)(OTf)_2]^+$.[90] Conversely, both solid state and solution analyses of complexes **3** and **4** are indicative of 4 or 5-coordinated species in a distorted TBP geometry. In particular, only one nitrile molecule is coordinated to the iron centre for complex **3**, probably as a result of steric effects by amino–

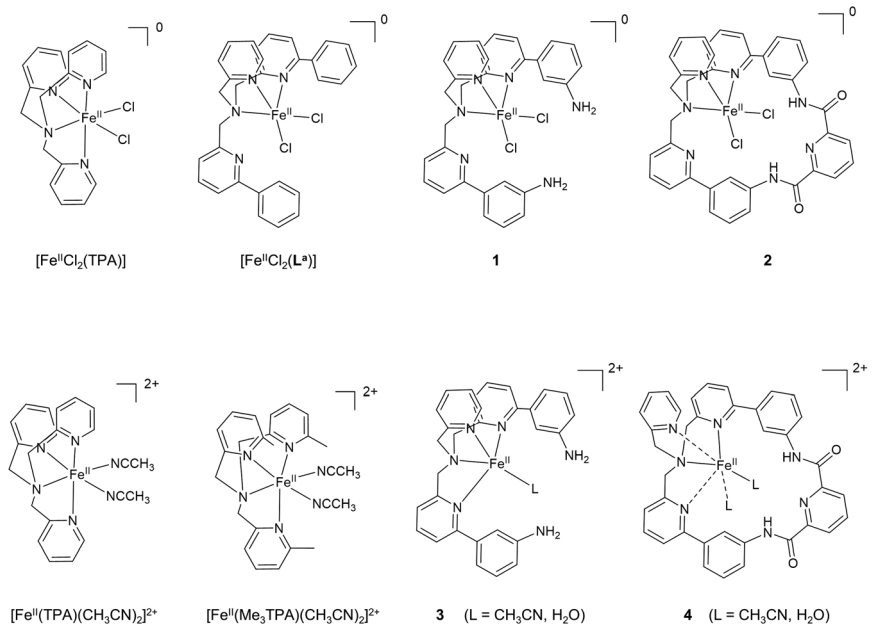

Scheme 7 Proposed structures for complexes **1**, **2**, **3** and **4** and their analogues in acetonitrile.

phenyl groups. For complex **4**, the absence of a signal at 120 ppm in the ^{1}H NMR spectrum suggests that the unsubstituted pyridyl is not bound to Fe^{II}, thus leading possibly to the coordination of the two substituted pyridyl groups and/or solvent. Such a structure remains however hypothetical without clear experimental evidence.

Discussion on the catalytic properties of complexes 1–4

Non-hemic iron(II) complexes of the general formula $LFe^{II}X_n$ (L = N-ligand, X = solvent or anion; n = 1, 2) are well known for reacting with H_2O_2 to yield Fe^{III}(OOH) species.[2,7,79] Depending on the nature of L and X, the resulting hydroperoxo can either react with a hydrogenated substrate (RH, pathway a, Scheme 8) or evolve towards Fe^{V}(O) (pathway b) or Fe^{IV}(O) (pathway c) species through heterolytic or homolytic O–O bond cleavage. Hence, these three transient species can potentially oxidize hydrogenated substrates. Notably, numerous studies have emphasized that oxidizing Fe^{V}(O)(OH) species could be obtained through a water-assisted process for complexes bearing strong field tetradentate aminopyridine ligands and two *cis*-labile sites.[2,79] Here, we have shown that the reaction of **2** with H_2O_2 leads possibly to the formation of the hydroperoxo complex according to UV-Vis spectroscopic data. In the absence of a substrate, the complex evolves towards the bis(μ-OH) species **2′** bearing a phenoxo moiety (Scheme 8). Such intramolecular aromatic hydroxylation was previously observed for $[Fe^{II}(6\text{-PhTPA})(CH_3CN)_2]^{2+}$ in the presence of ^{t}BuOOH in acetonitrile and was ascribed to the formation of a Fe(IV)-oxo species upon homolytic O–O bond breaking of the generated $[Fe^{II}(6\text{-PhTPA})(OO^tBu)]^{2+}$ adduct.[82] It was also described for other mononuclear complexes.[91,92]

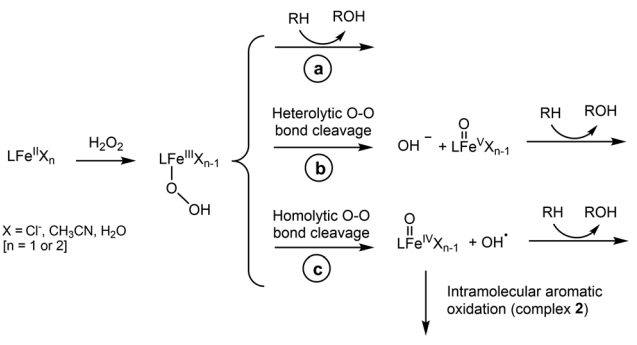

Scheme 8 Possible mechanistic pathways for the reaction of complexes **1**, **2**, **3** and **4** with H_2O_2, in the presence or absence of cyclohexane (RH), according to the catalytic studies.

Under catalytic conditions (1000 eq. of H_2O_2 and substrate *vs.* catalyst), all complexes lead to the formation of cyclohexanol (A) and cyclohexanone (K) with low yields (<1%) and low TONs. In particular, the ratio of produced alcohol over ketone (A/K) is close to 1, thus strongly suggesting a Fenton-like reaction for which the effective oxidant is a hydroxyl radical OH$^\bullet$, and not an iron–oxygen adduct.[7,90,93,94] This is consistent with the studies without a substrate: according to Scheme 8, pathway c leads to the formation of an Fe(IV)-oxo species and a hydroxyl radical. While the former can perform the intramolecular aromatic hydroxylation, the latter is involved in exogenous cyclohexane oxidation. It is noticeable that both macrocyclic complexes **2** and **4** are more efficient than **1** and **3**, and that the counter ion (Cl^- or OTf^-) does not significantly influence the results (Fig. 7). This would indicate that the rate-determining step is not the formation of the putative iron-hydroperoxo species but merely the homolytic O–O bond clea-

vage. The higher activity of **2** can be explained by the probable higher redox potential according to the electrochemical studies (see Table 4). Addition of acetic acid to promote pathway b was not conclusive since the TON substantially decreased (Fig. 7). Probably, the formation of the $Fe^{V}(O)$ is not enhanced for steric reasons, and the acetic acid then plays the role of a substrate (*vs.* $OH^{\bullet}$), thus inhibiting cyclohexane oxidation.

The reaction between *m*-CPBA and iron(II) complexes is well known for leading to the direct formation of iron(IV) and iron(V)-oxo species through homolytic and heterolytic O–O bond cleavage of the *m*-CPBA–iron adduct.[95] Here, we have shown that complex **3** presumably yields the transient species $[Fe^{IV}(O)(\mathbf{L^1})]^{2+}$ by reaction with *m*-CPBA in acetonitrile (Scheme 9). Moreover, our studies clearly demonstrate that complexes **1** and **2** behave differently from **3** and **4** for the catalytic oxidation of cyclohexane in the presence of *m*-CPBA. As shown in Fig. 8 and Table 6, complexes **1** and **2** perform the oxidation of cyclohexane into cyclohexanol and cyclohexanone with A/K > 1, whereas complexes **3** and **4** do essentially not. Intuitively, these discrepancies can be associated with the effect of the presence/absence of chloride ion(s) bound to the iron centre. Such an effect was previously reported for the reaction of different iron–porphyrin complexes in organic solvents. Indeed, Nam *et al.* showed that the strong electron-donating chloride ligand could enhance the reactivity of the Fe(III)–OOC(O)R adduct toward cyclohexane.[95] In contrast, the weak-donating triflate anion led to the formation of Fe(IV)-oxo species by homolytic O–O bond breaking. Such a scenario could be envisaged for complexes **1–4**. As shown in Scheme 9, the putative Fe^{III}(OOCOR) adduct may react with cyclohexane or evolve towards an Fe^{IV}-oxo complex, depending on the nature of the exogenously bound ligand (X = Cl^-, CH_3CN or H_2O). Thus, chloride ligands would promote the reaction of the acylperoxo species with cyclohexane while triflate ones would yield poorly reactive Fe(IV)-oxo species. Such metal-based oxidation (and not $OH^{\bullet}$) could be confirmed by the A/K ratio obtained for the catalytic studies, which varies between 0.9 and 4.5. Notably, the best results for catalysis have been obtained with complex **2**. These results are consistent with electrochemical data which indicate a relatively high oxidation potential for the macrocyclic complex (Table 4).

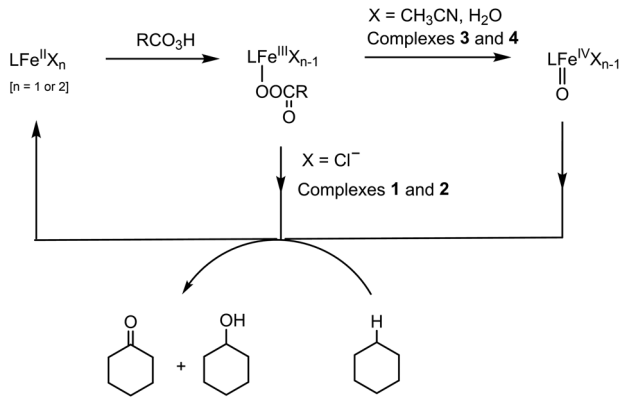

Scheme 9 Two proposed mechanistic pathways for the oxidation of cyclohexane by **1**, **2**, **3** or **4** in the presence of *m*-CPBA according to the catalytic studies.

Conclusions

In summary, we have synthesized and characterized four mononuclear iron(II) complexes, on the basis of the non-macrocyclic and macrocyclic ligands $\mathbf{L^1}$ and $\mathbf{L^2}$, respectively. Our studies provide evidence that all synthesized complexes are high-spin and mainly pentacoordinated in the solid state and in acetonitrile. The Fe^{II} centre is coordinated by three or four nitrogen atoms of the TPA core, the coordination sphere being completed by counter-anions (Cl^-, OTf^-) or solvent molecules (H_2O, CH_3CN). The penta-coordinated feature is probably due to steric constraints between the phenyl groups. The reaction of the different complexes with oxidizing agents (H_2O_2 and *m*-CPBA) leads presumably to the formation of hydroperoxo and oxo adducts as shown by UV-Vis spectroscopy. The catalytic studies of the oxidation of cyclohexane suggest a Fenton-like reaction involving a hydroxyl radical for all complexes when using H_2O_2 as the oxidant. It is noteworthy that a different scenario involving a metal-based reaction takes place when using *m*-CPBA. Hence, our studies demonstrate that two factors impact significantly the catalytic properties for the oxidation of cyclohexane. The first one is the macrocyclic design of the TPA-derived ligand which leads to higher catalytic activity. Such an effect could result from the high redox potential of complex **2** *vs.* non-macrocyclic analogues, as shown by electrochemical studies. The second parameter is the nature of the exogenous ligand (chloride, H_2O, CH_3CN) in solution which can control the reaction pathway. From this basis, future work will aim at introducing a second metal ion with the macrocyclic ligand $\mathbf{L^2}$ in order to mimic the dinuclear centre in the active site of sMMOs.

Conflicts of interest

There are no conflicts to declare.

Acknowledgements

The authors acknowledge the University of Bretagne Occidentale (UBO) for a PhD grant (M. Ayad). Dr Francois Michaud is thanked for X-ray diffraction analysis. The Agence Nationale de la Recherche (ANR-11-BS07-0024) is thanked for financial support.

Notes and references

1 S. Friedle, E. Reisner and S. J. Lippard, *Chem. Soc. Rev.*, 2010, **39**, 2768–2779.

2 I. Gamba, Z. Codolà, J. Lloret-Fillol and M. Costas, *Coord. Chem. Rev.*, 2017, **334**, 2–24.
3 W. Wang, A. D. Liang and S. J. Lippard, *Acc. Chem. Res.*, 2015, **48**, 2632–2639.
4 T. L. Poulos, *Chem. Rev.*, 2014, **114**, 3919–3962.
5 I. G. Denisov, T. M. Makris, S. G. Sligar and I. Schlichting, *Chem. Rev.*, 2005, **105**, 2253–2277.
6 B. Meunier, S. P. de Visser and S. Shaik, *Chem. Rev.*, 2004, **104**, 3947–3980.
7 A. C. Lindhorst, S. Haslinger and F. E. Kühn, *Chem. Commun.*, 2015, **51**, 17193–17212.
8 M. Costas, *Coord. Chem. Rev.*, 2011, **255**, 2912–2932.
9 A. J. Jasniewski and L. Que Jr., *Chem. Rev.*, 2018, **118**, 2554–2592.
10 E. I. Solomon, T. C. Brunold, M. I. Davis, J. N. Kemsley, S.-K. Lee, N. Lehnert, F. Neese, A. J. Skulan, Y.-S. Yang and J. Zhou, *Chem. Rev.*, 2000, **100**, 235–350.
11 E. I. Solomon, K. M. Light, L. V. Liu, M. Srnec and S. D. Wong, *Acc. Chem. Res.*, 2013, **46**, 2725–2739.
12 E. I. Solomon, S. Goudarzi and K. D. Sutherlin, *Biochemistry*, 2016, **55**, 6363–6374.
13 M. Costas, M. P. Mehn, M. P. Jensen and L. Que Jr., *Chem. Rev.*, 2004, **104**, 939–986.
14 E. G. Kovaleva and J. D. Lipscomb, *Nat. Chem. Biol.*, 2008, **4**, 186–193.
15 S. M. Barry and G. L. Challis, *ACS Catal.*, 2013, **3**, 2362–2370.
16 D. J. Ferraro, L. Gakhar and S. Ramaswamy, *Biochem. Biophys. Res. Commun.*, 2005, **338**, 175–190.
17 C. E. Tinberg and S. J. Lippard, *Acc. Chem. Res.*, 2011, **44**, 280–288.
18 A. Trehoux, J.-P. Mahy and F. Avenier, *Coord. Chem. Rev.*, 2016, **322**, 142–158.
19 R. Banerjee, Y. Proshlyakov, J. D. Lipscomb and D. A. Proshlyakov, *Nature*, 2015, **518**, 431–434.
20 H.-F. Hsu, Y. Dong, L. Shu, V. G. Young and L. Que, *J. Am. Chem. Soc.*, 1999, **121**, 5230–5237.
21 G. Xue, R. De Hont, E. Münck and L. Que Jr., *Nat. Chem.*, 2010, **2**, 400–405.
22 J.-U. Rohde, J.-H. In, M. H. Lim, W. W. Brennessel, M. R. Bukowski, A. Stubna, E. Münck, W. Nam and L. Que Jr., *Science*, 2003, **299**, 1037–1039.
23 W. Nam, Y.-M. Lee and S. Fukuzumi, *Acc. Chem. Res.*, 2014, **47**, 1146–1154.
24 W. Nam, *Acc. Chem. Res.*, 2015, **48**, 2415–2423.
25 J. Cho, S. Jeon, S. A. Wilson, L. V. Liu, E. A. Kang, J. J. Braymer, M. H. Lim, B. Hedman, K. O. Hodgson, J. S. Valentine, E. I. Solomon and W. Nam, *Nature*, 2011, **478**, 502–505.
26 A. Thibon, J. England, M. Martinho, V. G. Young, J. R. Frisch, R. Guillot, J.-J. Girerd, E. Münck, L. Que and F. Banse, *Angew. Chem., Int. Ed.*, 2008, **47**, 7064–7067.
27 A. Company, L. Gómez, X. Fontrodona, X. Ribas and M. Costas, *Chem. – Eur. J.*, 2008, **14**, 5727–5731.
28 I. Prat, J. S. Mathieson, M. Güell, X. Ribas, J. M. Luis, L. Cronin and M. Costas, *Nat. Chem.*, 2011, **3**, 788–793.
29 T. Inomata, K. Shinozaki, Y. Hayashi, H. Arii, Y. Funahashi, T. Ozawa and H. Masuda, *Chem. Commun.*, 2008, 392–394.
30 J. B. Strautmann, S. Dammers, T. Limpke, J. Parthier, T. P. Zimmermann, S. Walleck, G. Heinze-Bruckner, A. Stammler, H. Bogge and T. Glaser, *Dalton Trans.*, 2016, **45**, 3340–3361.
31 M. Kodera, M. Itoh, K. Kano, T. Funabiki and M. Reglier, *Angew. Chem., Int. Ed.*, 2005, **44**, 7104–7106.
32 M. Sekino, H. Furutachi, K. Tasaki, T. Ishikawa, S. Mori, S. Fujinami, S. Akine, Y. Sakata, T. Nomura, T. Ogura, T. Kitagawa and M. Suzuki, *Dalton Trans.*, 2016, **45**, 469–473.
33 M. Kodera, T. Tsuji, T. Yasunaga, Y. Kawahara, T. Hirano, Y. Hitomi, T. Nomura, T. Ogura, Y. Kobayashi, P. K. Sajith, Y. Shiota and K. Yoshizawa, *Chem. Sci.*, 2014, **5**, 2282–2292.
34 M. Kodera, S. Ishiga, T. Tsuji, K. Sakurai, Y. Hitomi, Y. Shiota, P. K. Sajith, K. Yoshizawa, K. Mieda and T. Ogura, *Chem. – Eur. J.*, 2016, **22**, 5924–5936.
35 L. H. Do and S. J. Lippard, *J. Am. Chem. Soc.*, 2011, **133**, 10568–10581.
36 L. H. Do and S. J. Lippard, *J. Inorg. Biochem.*, 2011, **105**, 1774–1785.
37 F. Wang, S. Becker, M. A. Minier, A. Loas, M. N. Jackson and S. J. Lippard, *Inorg. Chem.*, 2017, **56**, 11050–11058.
38 M. Mitra, J. Lloret-Fillol, M. Haukka, M. Costas and E. Nordlander, *Chem. Commun.*, 2014, **50**, 1408–1410.
39 M. Puri and L. Que Jr., *Acc. Chem. Res.*, 2015, **48**, 2443–2452.
40 D. Mandon, A. Machkour, S. Goetz and R. Welter, *Inorg. Chem.*, 2002, **41**, 5364–5372.
41 A. Machkour, D. Mandon, M. Lachkar and R. Welter, *Inorg. Chem.*, 2004, **43**, 1545–1550.
42 A. Machkour, D. Mandon, M. Lachkar and R. Welter, *Inorg. Chim. Acta*, 2005, **358**, 839–843.
43 N. K. Thallaj, A. Machkour, D. Mandon and R. Welter, *New J. Chem.*, 2005, **29**, 1555–1558.
44 L. Benhamou, M. Lachkar, D. Mandon and R. Welter, *Dalton Trans.*, 2008, 6996–7003.
45 N. K. Thallaj, O. Rotthaus, L. Benhamou, N. Humbert, M. Elhabiri, M. Lachkar, R. Welter, A. M. Albrecht-Gary and D. Mandon, *Chem. – Eur. J.*, 2008, **14**, 6742–6753.
46 L. Benhamou, A. Machkour, O. Rotthaus, M. Lachkar, R. Welter and D. Mandon, *Inorg. Chem.*, 2009, **48**, 4777–4786.
47 A. Wane, N. K. Thallaj and D. Mandon, *Chem. – Eur. J.*, 2009, **15**, 10593–10602.
48 H. Jaafar, R. Louis and D. Mandon, *Inorg. Chim. Acta*, 2011, **366**, 147–153.
49 H. Jaafar, B. Vileno, A. Thibon and D. Mandon, *Dalton Trans.*, 2011, **40**, 92–106.
50 D. Mandon, H. Jaafar and A. Thibon, *New J. Chem.*, 2011, **35**, 1986–2000.
51 D. Huang and R. H. Holm, *J. Am. Chem. Soc.*, 2010, **132**, 4693–4701.
52 X. Zhang, D. Huang, Y. S. Chen and R. H. Holm, *Inorg. Chem.*, 2012, **51**, 11017–11029.

53 M. R. Halvagar, B. Neisen and W. B. Tolman, *Inorg. Chem.*, 2013, **52**, 793–799.
54 S. M. Nelson and J. Rodgers, *J. Chem. Soc. A*, 1968, 272–276.
55 W. Offermann and F. Vögtle, *Angew. Chem., Int. Ed. Engl.*, 1980, **19**, 464–465.
56 Z. Tyeklar, R. R. Jacobson, N. Wei, N. N. Murthy, J. Zubieta and K. D. Karlin, *J. Am. Chem. Soc.*, 1993, **115**, 2677–2689.
57 C.-L. Chuang, O. dos Santos, X. Xu and J. W. Canary, *Inorg. Chem.*, 1997, **36**, 1967–1972.
58 D. Mandon, A. Nopper, T. Litrol and S. Goetz, *Inorg. Chem.*, 2001, **40**, 4803–4806.
59 M. P. Jensen, S. J. Lange, M. P. Mehn, E. L. Que and L. Que Jr., *J. Am. Chem. Soc.*, 2003, **125**, 2113–2128.
60 C. Piguet, *J. Chem. Educ.*, 1997, **74**, 815.
61 G. A. Bain and J. F. Berry, *J. Chem. Educ.*, 2008, **85**, 532.
62 G. Shedrix, *SHELXS97*, University of Gottingen, Germany, 1997.
63 L. J. Farrugia, *J. Appl. Crystallogr.*, 1999, **32**, 837–838.
64 A. Diebold and K. S. Hagen, *Inorg. Chem.*, 1998, **37**, 215–223.
65 A. Machkour, N. K. Thallaj, L. Benhamou, M. Lachkar and D. Mandon, *Chem. – Eur. J.*, 2006, **12**, 6660–6668.
66 L. Benhamou, H. Jaafar, A. Thibon, M. Lachkar and D. Mandon, *Inorg. Chim. Acta*, 2011, **373**, 195–200.
67 L. Benhamou, A. Thibon, L. Brelot, M. Lachkar and D. Mandon, *Dalton Trans.*, 2012, **41**, 14369–14380.
68 A. Thibon, L. Karmazin-Brelot and D. Mandon, *Eur. J. Inorg. Chem.*, 2013, **2013**, 1118–1122.
69 N. K. Thallaj, P. Y. Orain, A. Thibon, M. Sandroni, R. Welter and D. Mandon, *Inorg. Chem.*, 2014, **53**, 7824–7836.
70 A. W. Addison, T. N. Rao, J. Reedijk, J. van Rijn and G. C. Verschoor, *J. Chem. Soc., Dalton Trans.*, 1984, 1349–1356.
71 W. J. Geary, *Coord. Chem. Rev.*, 1971, **7**, 81–122.
72 T. J. Hubin, J. M. McCormick, S. R. Collinson, M. Buchalova, C. M. Perkins, N. W. Alcock, P. K. Kahol, A. Raghunathan and D. H. Busch, *J. Am. Chem. Soc.*, 2000, **122**, 2512–2522.
73 D. B. Rorabacher, *Chem. Rev.*, 2004, **104**, 651–697.
74 H. Nagao, N. Komeda, M. Mukaida, M. Suzuki and K. Tanaka, *Inorg. Chem.*, 1996, **35**, 6809–6815.
75 C.-L. Chuang, K. Lim, Q. Chen, J. Zubieta and J. W. Canary, *Inorg. Chem.*, 1995, **34**, 2562–2568.
76 R. J. Butcher and A. W. Addison, *Inorg. Chim. Acta*, 1989, **158**, 211–215.
77 G. J. Britovsek, J. England and A. J. White, *Inorg. Chem.*, 2005, **44**, 8125–8134.
78 D. M. Kurtz, *Chem. Rev.*, 1990, **90**, 585–606.
79 S. M. Hölzl, P. J. Altmann, J. W. Kück and F. E. Kühn, *Coord. Chem. Rev.*, 2017, **352**, 517–536.
80 A. J. Simaan, S. Döpner, F. Banse, S. Bourcier, G. Bouchoux, A. Boussac, P. Hildebrandt and J.-J. Girerd, *Eur. J. Inorg. Chem.*, 2000, **2000**, 1627–1633.
81 J. Wang, M. S. Mashuta, Z. Sun, J. F. Richardson, D. N. Hendrickson and R. M. Buchanan, *Inorg. Chem.*, 1996, **35**, 6642–6643.
82 S. J. Lange, H. Miyake and L. Que, *J. Am. Chem. Soc.*, 1999, **121**, 6330–6331.
83 P. Gomez-Romero, E. H. Witten, W. M. Reiff, G. Backes, J. Sanders-Loehr and G. B. Jameson, *J. Am. Chem. Soc.*, 1989, **111**, 9039–9047.
84 E. N. Chygorin, S. R. Petrusenko, V. N. Kokozay, Y. O. Smal, I. V. Omelchenko and O. V. Shishkin, *Acta Crystallogr., Sect. E: Struct. Rep. Online*, 2011, **67**, m1563–m1564.
85 C. Ling, L. Song and X. Wang, *Acta Crystallogr., Sect. E: Struct. Rep. Online*, 2011, **67**, m1232–m1233.
86 M. H. Lim, J. U. Rohde, A. Stubna, M. R. Bukowski, M. Costas, R. Y. Ho, E. Munck, W. Nam and L. Que Jr., *Proc. Natl. Acad. Sci. U. S. A.*, 2003, **100**, 3665–3670.
87 T. K. Paine, M. Costas, J. Kaizer and L. Que Jr., *J. Biol. Inorg. Chem.*, 2006, **11**, 272–276.
88 J. Serrano-Plana, F. Acuna-Pares, V. Dantignana, W. N. Oloo, E. Castillo, A. Draksharapu, C. J. Whiteoak, V. Martin-Diaconescu, M. G. Basallote, J. M. Luis, L. Que Jr., M. Costas and A. Company, *Chem. – Eur. J.*, 2018, **24**, 5331–5340.
89 Y. Zang, J. Kim, Y. Dong, E. C. Wilkinson, E. H. Appelman and L. Que, *J. Am. Chem. Soc.*, 1997, **119**, 4197–4205.
90 K. Chen and L. Que, *J. Am. Chem. Soc.*, 2001, **123**, 6327–6337.
91 Y. Mekmouche, S. Ménage, C. Toia-Duboc, M. Fontecave, J.-B. Galey, C. Lebrun and J. Pécaut, *Angew. Chem., Int. Ed.*, 2001, **40**, 949–952.
92 Y. Mekmouche, S. Ménage, J. Pécaut, C. Lebrun, L. Reilly, V. Schuenemann, A. Trautwein and M. Fontecave, *Eur. J. Inorg. Chem.*, 2004, **2004**, 3163–3171.
93 E. P. Talsi and K. P. Bryliakov, *Coord. Chem. Rev.*, 2012, **256**, 1418–1434.
94 A. Thibon, V. Jollet, C. Ribal, K. Senechal-David, L. Billon, A. B. Sorokin and F. Banse, *Chem. – Eur. J.*, 2012, **18**, 2715–2724.
95 W. Nam, M. H. Lim, S. K. Moon and C. Kim, *J. Am. Chem. Soc.*, 2000, **122**, 10805–10809.